Targeting hTERT Promoter G-Quadruplex DNA Structures with Small-Molecule Ligand to downregulate hTERT Expression for Triple-Negative Breast Cancer Therapy

Wei Long[1], Yao-Xun Zeng[1], Bo-Xin Zheng[1], Yu-Bo Li[2], Ya-Kun Wang[1], Ka-Hin Chan[1], Meng-Ting She[1], Yu-Jing Lu*[,3], Chunyang Cao*[,2] and Wing-Leung Wong*[,1]

[1] State Key Laboratory of Chemical Biology and Drug Discovery, Department of Applied Biology and Chemical Technology, The Hong Kong Polytechnic University, Hung Hom, Kowloon, Hong Kong SAR 999077, China.

[2] State Key Laboratory of Chemical Biology, Shanghai Institute of Organic Chemistry, Chinese Academy of Sciences, 345 Lingling Road, Shanghai, 200032, China.

[3] School of Biomedical and Pharmaceutical Sciences, Guangdong University of Technology, Guangzhou 510006, China.

* Corresponding author

E-mail (YJL): luyj@gdut.edu.cn

E-mail (CYC): ccao@mail.sioc.ac.cn

E-mail (WLW): wing.leung.wong@polyu.edu.hk

ABSTRACT

The human telomerase reverse transcriptase (hTERT) may have noncanonical functions in transcriptional regulation and metabolic reprogramming in cancer cells, but it is a challenging target. We thus developed small-molecule ligands targeting hTERT promoter G-quadruplex DNA structures (hTERT G4) to downregulate hTERT expression. Ligand **5** showed high affinity towards hTERT G4 (K_d=1.1 μM) and potent activity against triple-negative breast cancer cells (MDA-MB-231, IC_{50}=1 μM). In cell-based assays, **5** not only exerts markedly inhibitory activity on classical telomere functions including decreased telomerase activity, shortened telomere length and cellular senescence, but also induces DNA damage, acute cellular senescence and apoptosis. This study reveals that hTERT G4-targeting ligand may cause mitochondrial dysfunction, disrupt iron metabolism and activate ferroptosis in cancer cells. The *in vivo* antitumor efficacy of **5** was also evaluated in an MDA-MB-231 xenograft mouse model and approximately 78.7% tumor weight reduction was achieved. No observable toxicity against the major organs was observed.

1. INTRODUCTION

Cell proliferation and survival are highly dependent on telomerase expression and maintenance of telomere length. The human telomerase reverse transcriptase (hTERT) serves as a catalytic subunit of telomerase. The transcription and expression of *hTERT* gene is silent in mature differentiated normal somatic cells.[1] However, telomerase silencing in most cancer cells (85-90% of cancer specimens) is usually abolished by mutations in hTERT promoter, and thus the activated telomerase allows cancer cells to proliferate indefinitely by maintaining telomere length.[2–4] The role of telomeres and the mechanism of their maintenance have been well studied.[1–7] Telomere length shortening is known a key driver of induced chromosomal and genomic instability, and the transcriptional regulation of hTERT is thought to play an important role in telomerase activation in cancer.[2] However, the noncanonical function of hTERT (non-telomerase functions) remains unclear.

Telomere lengthening is generally thought to be the primary function of reactivated hTERT, but this activity cannot explain all biological effects observed in cancer biology including the markedly increased cell proliferation, resistance to apoptosis and invasion. Therefore, some studies report that hTERT may carry out certain noncanonical functions including transcriptional regulation and metabolic reprogramming that supports cancer cell proliferation, invasion and the development of resistance.[5–10] Recent studies also suggest that hTERT could directly regulate certain vital features of cancer and thus hTERT is currently considered as a central regulator in anticancer research.[11–17] The development of novel anticancer strategy to regulate the expression of hTERT and its noncanonical functions is challenging but it may provide new and effective therapeutics against drug resistant and invasive cancers such as triple-negative breast cancer (TNBC).

At present, a number of approaches targeting telomerase have been attempted, including gene therapy,[18] antisense oligonucleotides,[19,20] immunotherapy,[21,22] and small-molecule inhibitors;[23,24] however, the noncanonical function of hTERT is not inhibited. In principle, to inhibit the hTERT function is a viable mechanism for anticancer therapy because both canonical and noncanonical functions of hTERT can be suppressed simultaneously with inhibitors. Nonetheless, none hTERT inhibitor is currently available because hTERT is a challenging drug target. To explore other promising alternatives for cancer therapy, G-quadruplex structures (G4s) has been an emerging target of small molecules and recent evidences also support that G4s are highly enriched in certain cellular regions such as telomeres, gene promoters, and the 5-terminal untranslated region of mRNAs.[25–27]

It has been reported that the oncogene, *hTERT*, encoding the reverse transcriptase component of the human telomerase ribonucleoprotein complex, can form G4s *in vitro*.[28–31] The transcription factor depending on hTERT promoter G4-forming sequences for regulating hTERT's telomere and non-telomere functions have also been reported recently.[32,33] Thus, the hTERT G4 is a potential target for chemical biology and anticancer study. The hTERT G4-DNA targeting ligands with high affinity may inhibit the expression of hTERT. Consequently, both canonical and noncanonical functions of hTERT could be repressed. This approach could be a promising strategy to treat drug-resistant cancers.

Currently, several small-molecule ligands targeting telomeric G4-structures, including the widely recognized ligands TMPyP4,[34] telomere repressor,[35] BRACO-19,[36] and RHPS4,[37] have been reported to show potent inhibitory effects in various tumor cells and xenograft mice models. Nonetheless, the design of small-sized molecular ligands selectively targeting hTERT G4 is not well-established. Only few ligands can be found in literature. For instance, GTC365 targeting the major G4 in the hTERT promoter, developed by Hurley and co-workers, exerted inhibitory effects on telomerase activity.[30,38] In addition, SOP1812, reported by Neidle and co-workers, showed strong affinity for both human telomeres and hTERT G4.[39] These prior arts support that hTERT G4 is a potential anticancer drug target of small-molecule ligands.

In the present study, we attempted to design potent hTERT G4-targeting ligands. We selected thiazole orange (TO) as the core skeleton for ligand modification because some previous studies demonstrated that TO scaffold could be tailored to target certain types of G4s with high affinity and give enhanced fluorescent signal for molecular interactions.[40,41] A series of TO ligands substituted with an indolyl group were thus developed for in-depth investigation on the effects of selectivity targeting hTERT G4-DNA structure and anticancer activity. Our results shown that ligand **5** was selectively binding to hTERT G4 with a strong affinity (K_d = 1.1 μM) and it markedly increased the *in vitro* stability of hTERT G4 (ΔT_m = 11.7 °C). The cell-based assays also showed that the ligand effectively repressed *hTERT* gene transcription, downregulated hTERT expression, and caused cancer cell senescence, cell cycle arrest, autophagy, DNA damage, oxidative stress, ferroptosis and apoptosis. Furthermore, the *in vivo* antitumor efficacy of **5** was demonstrated in an MDA-MB-231 xenograft mouse model. For a 16-day treatment with **5** (dose of 5 mg/kg, every 2-day), 78.7% tumor weight reduction was achieved. The **5**-treated mice showed no observable toxicity against the major organs examined. The present study may provide new insights into the design of potent hTERT G4-DNA

targeting anticancer agents against drug-resistant and aggressive cancers such as triple-negative breast cancer.

2. RESULTS AND DISCUSSION

2.1. Design of hTERT G4-DNA Targeting Small Molecule Ligands. We constructed rationally a series of new hTERT G4-bnding ligands, **1**–**10**, based on a parent scaffold of thiazole orange by introducing different terminal functional groups to regulate the polarity, rigidity and size of the molecular structure (Scheme 1). The ligands are designed to be non-emissive in solution under physiological conditions and they can generate markedly fluorescent signal upon interacting with hTERT G4 *in vitro* and in living cells. To investigate the selectivity of these ligands targeting hTERT G4, a panel of nucleic acid structures (**Table S1**) include single-stranded DNA, double-stranded DNA, promoter G4-DNA, telomere G4-DNA and hTERT antisense DNA were titrated with ligands **1**–**10** (Figure S1).

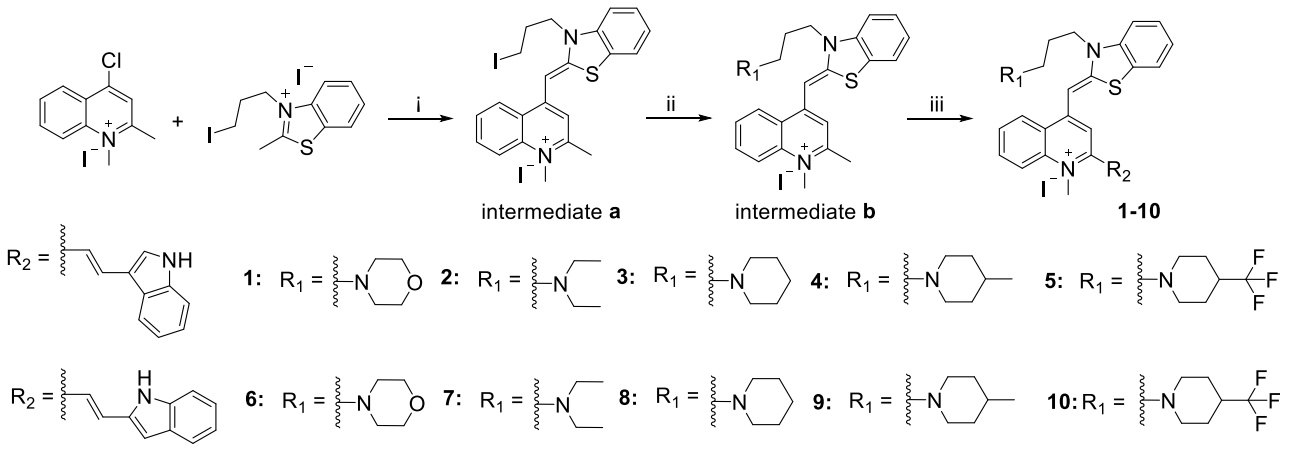

Scheme 1. Synthetic routes to compounds **1**–**10**. Reagents and conditions: (i) reaction with 3-(3-iodopropyl)-2-methylbenzo[d]thiazol-3-ium bromide, 40 °C, 3 h; (ii) reaction with morpholine, diethylamine, piperidine, 4-methylpiperidine or 4-(trimethyl-λ^4-fluoraneyl)piperidine, methanol, 40 °C, 24 h; (iii) reaction with 1*H*-indole-3-carbaldehyde or 1*H*-indole-2-carbaldehyde, acetonitrile, 105 °C, reflux 24 h.

Fluorescence titration results indicated that **5** exhibited the best selectivity toward hTERT G4 in terms of enhanced fluorescent signal for molecular interaction in pH7.4 Tris-HCl buffer. Ligand **5** interacted with hTERT G4 gave 29-fold (F/F_0) signal enhancement, which was 2-6 times of other G4-DNA substrates, 3 times of hTERT antisense DNA, 3 times of double-stranded DNA substrates, and 18 times of single-stranded DNA substrates (Figure 1A and Figure S2). Compared to its analogues, **5** generally shows better selectivity towards hTERT G4. It is probably due to its terminal functional

groups of CF_3 strengthening noncovalent interactions and the relatively more open indolyl moiety (substituted at 3-position compared to 2-position of the indole ring may has less steric hindrance) being favorable for hydrogen bonding interactions with the G4-target.

UV-Vis titrations also showed a new peak formation (Figure 1B) in concentration dependent manner when **5** was titrated with hTERT G4, indicating the formation of new adduct. Moreover, there was a markedly induced CD signal (420-550 nm) upon the interaction of **5** with hTERT G4 (Figure 1C and Figure S3). The unwinding temperature of the complex formed (ΔT_m = 11.7 °C) was much higher than that of other nucleic acids (Figure 1D and Figure S4). Furthermore, from the results of ITC experiments (Table 1, Figure 1E and Figure S5), **5** exhibited the highest affinity towards hTERT G4 (K_d = 1.1 μM) and it was notably stronger than that of telomeric G4 (Telo21: K_d = 3.3 μM), c-MYC G4 (Pu27: K_d = 14.7 μM), hTERT antisense DNA (*i*-hTERT, K_d = 2.8 μM), and double-stranded DNA (Ds26: K_d = 18.9 μM). Taken together, these biophysical results suggest that **5** may have better selective and affinity targeting hTERT G4.

From ITC titration assays, the binding stoichiometry of the **5**-hTERT G4 complex formed in solution is 3:1 (Table 1), indicating that the hTERT sequence (Figure 1F) may have three potential binding sites and each of them may interact with one ligand. To further confirm the interaction of **5** with hTERT G4 in solution, ^{1}H NMR titration study was performed. The guanine imino proton in the G-tetrad exhibits the typical chemical shifts in 10–12.5 ppm region.[42] The results support that the DNA sequence of PQS1, PQS2 and PQS3 can form G4-structure in a solution with 20 mM K^+ ion. The result is in accord with literature reports.[28–31] When **5** was added to the DNA solution (from 1:1 to 3:1 ratio), the ligand interacted with G-tetrad and the changes of these imino proton signals were clearly observed.[43] The remarkable shifts of several peaks in PQS1, PQS2, and PQS3 were observed in the titration. These results suggest that **5** may interact with the G-tetrads formed in PQS1, PQS2, and PQS3, respectively.

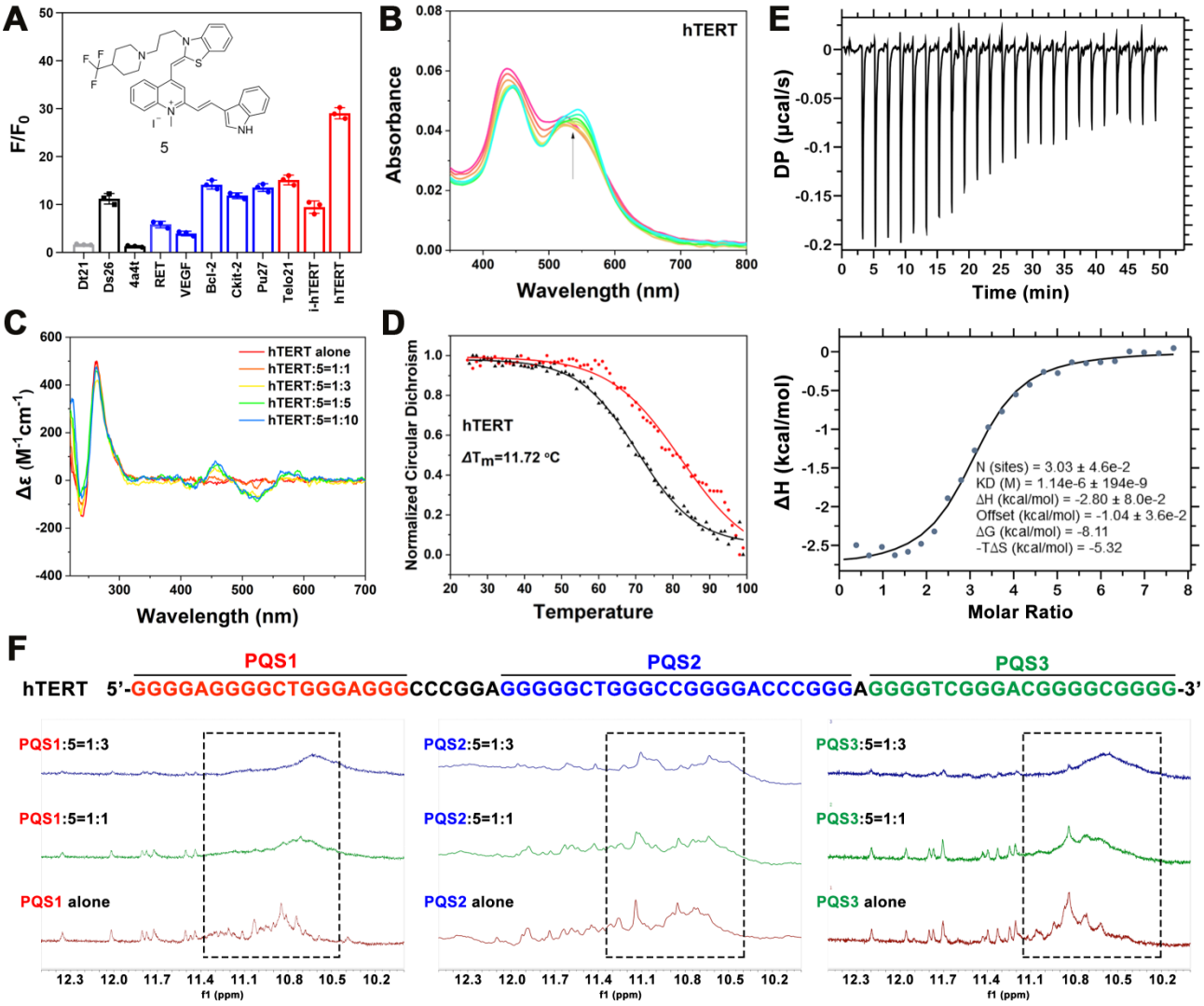

Figure 1. (A) Selectivity screening based on induced fluorescent responses of **5** (5 μM) upon bound with various nucleic acids (10 μM). (B) Ultraviolet Spectrophotometric titrations of **5** (5 μM) with hTERT G4-DNA (0–10 μM). (C) CD spectra of 5 μM hTERT G4-DNA binding with **5**. (D) CD melting curves for hTERT G4-DNA in the absence and presence of **5** (5 μM). (E) The binding of hTERT G4-DNA to **5** was studied by isothermal titration calorimetry (ITC). (F) Imino proton regions of ^{1}H NMR spectra showing the interaction PQS1, PQS2 or PQS3 with **5** at different molar ratio (1:0 to 1:3). The titration assays were performed in 25 mM KH_2PO_4 buffer (20 mM KCl, 10% D_2O, pH 7.4) using 600 MHz Bruker spectrometers at 25 °C.

Table 1. The Binding Parameters Obtained from Isothermal Titration Calorimetry (ITC) Study for ligand 5 Interacting with Different Nucleic Acid Structures at 25 °C

	ΔT_m	K_d (μM)	ΔH (kcal/mol)	ΔG (kcal/mol)	$-T\Delta S$	N (sites)
Dt21	-2.51±0.12	n.d.	n.d.	n.d.	n.d.	n.d.
4a4t	1.65±0.71	n.d.	n.d.	n.d.	n.d.	n.d.
Ds26	1.01±0.41	18.9±5.14	-1.32	-6.45	-4.84	2.32±0.11
VEGF	0.72±0.21	n.d.	n.d.	n.d.	n.d.	n.d.
RET	0.96±0.26	n.d.	n.d.	n.d.	n.d.	n.d.
Ckit-2	2.45±0.14	6.80±1.25	-1.59	-7.05	-5.34	2.79±0.08
Pu27	2.59±0.48	14.7±3.88	-2.44	-6.59	-3.8	3.76±0.26
Bcl-2	6.40±0.68	3.61±0.57	-2.34	-7.43	-4.96	1.69±0.04
Telo21	8.85±0.23	3.28±0.24	-1.09	-7.49	-6.37	3.04±0.03
i-hTERT	8.82±0.32	2.79±0.41	-1.2	-7.58	-6.33	2.73±0.05
hTERT	11.72±0.73	1.14±0.19	-2.72	-8.11	-5.32	3.03±0.05

n.d.: denotes not determined due to the ligand-DNA binding signal is too weak for estimation.

Table 2. Half-Maximal Inhibitory Concentration (IC_{50}, μM) of Ligands (1–10) against Human Cancer Cell Lines (A549, HeLa, PC3, HepG2, MDA-MB-231 and U2OS) and Noncancerous Cell Lines (HK-2 and HUEVC) with Incubation for 48 h

Ligand	A549	HeLa	PC3	HepG2	MDA-MB-231	U2OS	HK-2	HUEVC
1	2.1	2.3	4.7	5.8	2.9	7.8	5.8	16.5
2	2.3	1.9	5.4	4.7	2.1	9.4	4.6	14.5
3	1.7	1.8	3.8	4.5	3.1	5.1	5.4	11.9
4	1.7	1.9	2.4	3.2	1.9	5.3	5.5	6
5	2.1	2.6	2.5	2.9	1	3.9	9.4	8.7
6	5.0	4.1	4.8	5.2	6.4	14.8	9.5	16.6
7	4.7	3.3	3.1	5.4	5.6	10.3	9.5	11.9
8	3.6	3	3.3	4.5	3.3	5	7.9	9.4
9	4.3	3.1	2.5	5	2.6	6.2	6.3	8
10	6.6	5.5	3.9	4.7	5.3	9.8	14.7	12

2.2. Evaluation of Cytotoxicity of Ligands Against Human Cancer Cells and Noncancerous Cells. To investigate whether **5** showed broad-spectrum anticancer activity, we selected a number of telomerase-positive cancer cell lines (A549, HeLa, PC3, HepG2 and MDA-MB-231), an ALT (alterative lengthening of telomere) cancer cell line U2OS,[44] and nonmalignant cell lines (HK-2 and HUEVC) for evaluation (Table 2, Figure S6–S7). The IC_{50} values of **5** was found from 1–2.9 μM against the telomerase-positive cancer cells, while the IC_{50} value against U2OS (3.9 μM) was slightly higher but it was still effective. These results suggest that **5** is generally potent against both the telomerase activity dependent and independent cancer cells. Notably, the drug-resistant MDA-MB-231 breast cancer cell is more susceptible to **5** (IC_{50} = 1 μM), while the ligand has a relatively lower cytotoxicity against two nonmalignant cells examined (IC_{50} = 8.7–9.5 μM).

2.3. Study the Intracellular Location and Target of Ligand 5 in Living MDA-MB-231 Cancer Cells. Ligand **5** can generate intensive fluorescence upon interacting with hTERT G4 *in vitro* under physiological conditions. Thus, the enhanced fluorescent signal of **5** for molecular interactions allows us to investigate its cellular location and binding targets with confocal imaging techniques in living cancer cells. Since **5** shows high toxicity against MDA-MB-231, this cell line was selected for further assays. The live-cell images showed that **5** was primarily localized in the nucleus and subnuclear regions of the cells (Figure 2A, the green signal).

To further confirm that the intracellular target of **5** is DNA, enzymatic digestion assays were performed for **5**-treated MDA-MB-231 cells. The DNase I treatment removed almost all the fluorescence of both **5** (green) and Hoechst 33342 (blue) DNA imaging from the cells (Figure 2B). However, RNase A treatment did not cause observable reduction in the green fluorescence of **5**. The results indicate that **5** may primarily bind to DNA substrates in the nuclear region in living MDA-MB-231 cells. Moreover, the immunofluorescence staining with BG4 (a G4-specific antibody)[45] was found co-localized well with **5** (Figure 2C: BG4 (purple) and **5** (green)). The result supports that BG4 and **5** may bind to the same or similar cellular targets, indicating that **5** could possibly interact with G4-DNA in living MDA-MB-231 cells.

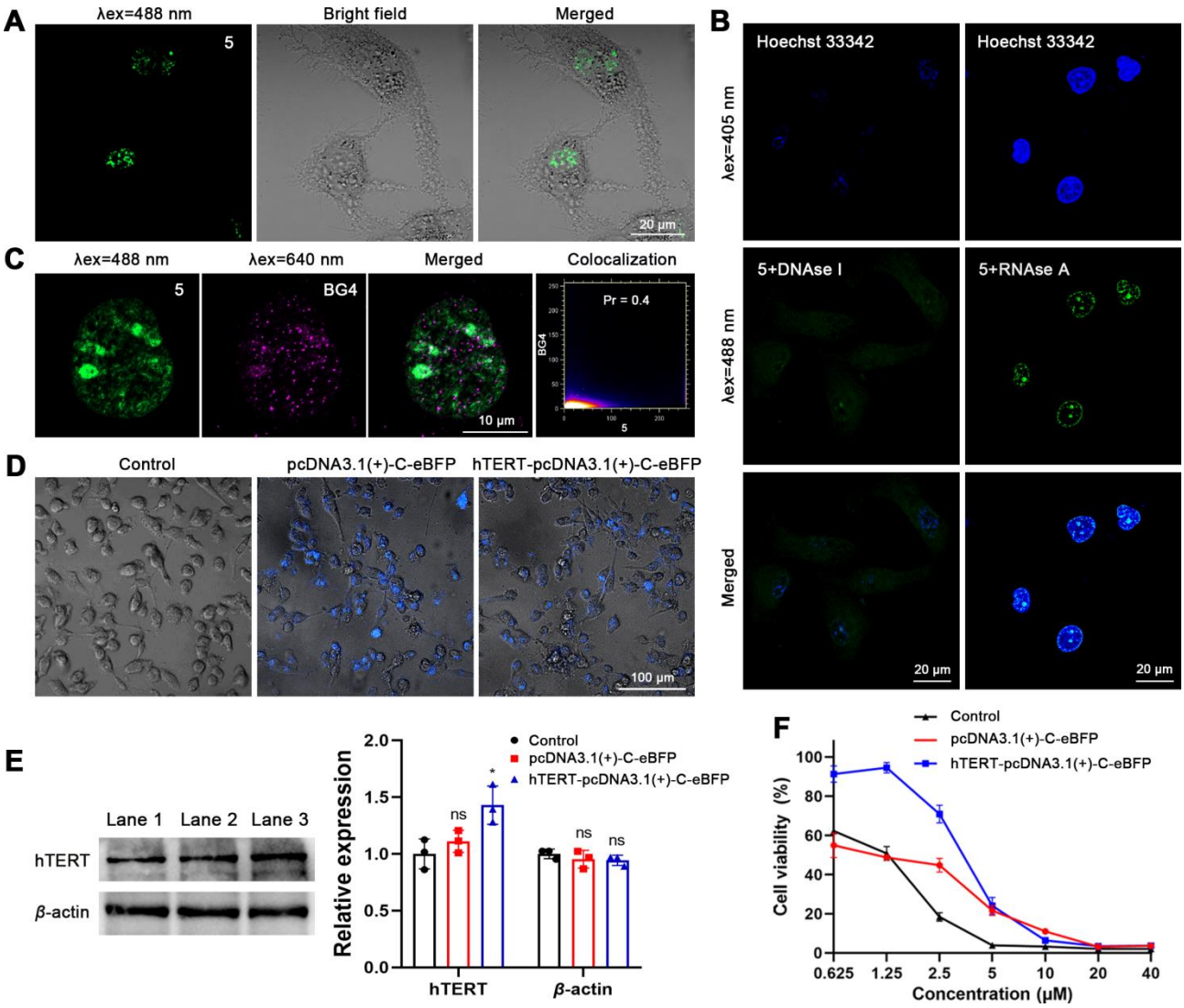

Figure 2. (A) Confocal microscope fluorescence images of live MDA-MB-231 cells stained with **5** (5 μM) for 10 min and Hoechst 33342 (1.0 μM) for 10 min. (B) Confocal microscope fluorescence images of fixed MDA-MB-231 cells stained with **5** (5 μM) and Hoechst 33342 (1.0 μM) for 10 min and then the cells were treated with DNase I or RNase A. (C) The co-localization study of BG4 and **5** (5 μM) in fixed MDA-MB-231 cells. (D) Imaging of MDA-MB-231 cells transfected with hTERT-pcDNA3.1(+)-C-eBFP plasmid and pcDNA3.1(+)-C-eBFP plasmid. (E) hTERT protein expression in MDA-MB-231 cells with hTERT-pcDNA3.1(+)-C-eBFP transfection. Lane 1: Cells with no transfection. Lane 2: Cells transfected with pcDNA3.1(+)-C-eBFP. Lane 3: Cells transfected with hTERT-pcDNA3.1(+)-C-eBFP. N = 3, mean ± SD, (*) $P < 0.05$, (**) $P < 0.01$, and (***) $P < 0.001$, significantly different from the control; ns, not significantly different from the control. (F) Cell viability of **5** to MDA-MB-231 cells transfected with hTERT-pcDNA3.1(+)-C-eBFP plasmid, pcDNA3.1(+)-C-eBFP plasmid or no transfection.

To obtain more cellular evidence to support the hypothesis that the primary target of **5** could be hTERT G4 and the anticancer activity of **5** observed could probably be attributed to the inhibition of hTERT expression, we transfected MDA-MB-231 cells with hTERT-pcDNA3.1(+)-C-eBFP overexpressing hTERT. The cell overexpressed hTERT is expected to alleviate the toxicity of **5**. The

blue fluorescent foci were observed in the transfected cells (Figure 2D), indicating that hTERT-pcDNA3.1(+)-C-eBFP was successfully transfected in MDA-MB-231 cells. The transfection efficiency was 70–80% approximately. We also used Western Blot assays to confirm that hTERT was overexpressed in the transfected cells (Figure 2E and Figure S8). As expected, the semi-inhibitory concentration of **5** (IC_{50} = 3.3 μM) against the transfected MDA-MB-231 cells was significantly higher than that of the control group (IC_{50} = 1.2 μM), suggesting that the ligand was being less toxic against the transfected MDA-MB-231 cells overexpressing hTERT (Figure 2F). These results indicate that **5** may interact with hTERT G4 and repress hTERT expression in MDA-MB-231 cells.

2.4. Ligand 5 Downregulates hTERT Expression and Inhibits Telomere Function in MDA-MB-231 Cells. It has been reported that the expression of the *hTERT* gene plays an important regulatory role in the growth of cancer cells.[16] The downregulation of hTERT expression may induce cancer cell death,[46] but the regulatory mechanism of hTERT is still unclear. We thus investigated the influence of telomere functions induced by **5** targeting hTERT G4 in MDA-MB-231 cells. The mRNA expression of *hTERT* and *c-MYC* genes in MDA-MB-231 cells treated with **5** was quantified by qRT-PCR (Figure 3A). The hTERT mRNA expression level was found significantly downregulated by **5** in a concentration-dependent manner (0–1.5 μM), while both c-MYC mRNA and CTCF mRNA (a regulatory factor in the promoter region of the gene)[47] were not significantly downregulated. These cellular results indicate that **5** may selectively target hTERT G4 in cancer cells and thus it inhibits hTERT expression at transcriptional level. Further Western Blot analysis confirmed that **5** inhibited the expression of hTERT and telomeric repeat binding factor 2 (TRF2) in a concentration-dependent manner (Figure 3B and Figure S9). TRF2 is a key telomere-capping protein and involves in the regulation of cellular activities and chromosome stability through the maintenance of telomere structure and the regulation of telomere length. It also plays important roles in the process of cellular aging and carcinogenesis.[48] Consequently, the telomere function and chromosome stability may be interrupted.[2]

Some recent studies suggest that hTERT may regulate directly the telomerase activity in cancer cells.[49] We thus studied the effect of **5** on telomerase activity in MDA-MB-231 cells with TRAP assays.[13] As expected, **5** at 1 μM (IC_{50} concentration) or above significantly inhibited telomerase activities (Figure 3C). Furthermore, MDA-MB-231 cells treated with **5** at 0.2 μM for 10 days exhibited a characteristic feature of cellular senescence, which was evidenced by both the positive

SA-β-gal staining (Figure 3D) and a significant telomere length shortening effect induced by the ligand (Figure 3E).[40] These results demonstrate that **5** may induce telomere dysfunction in MDA-MB-231 cancer cells.

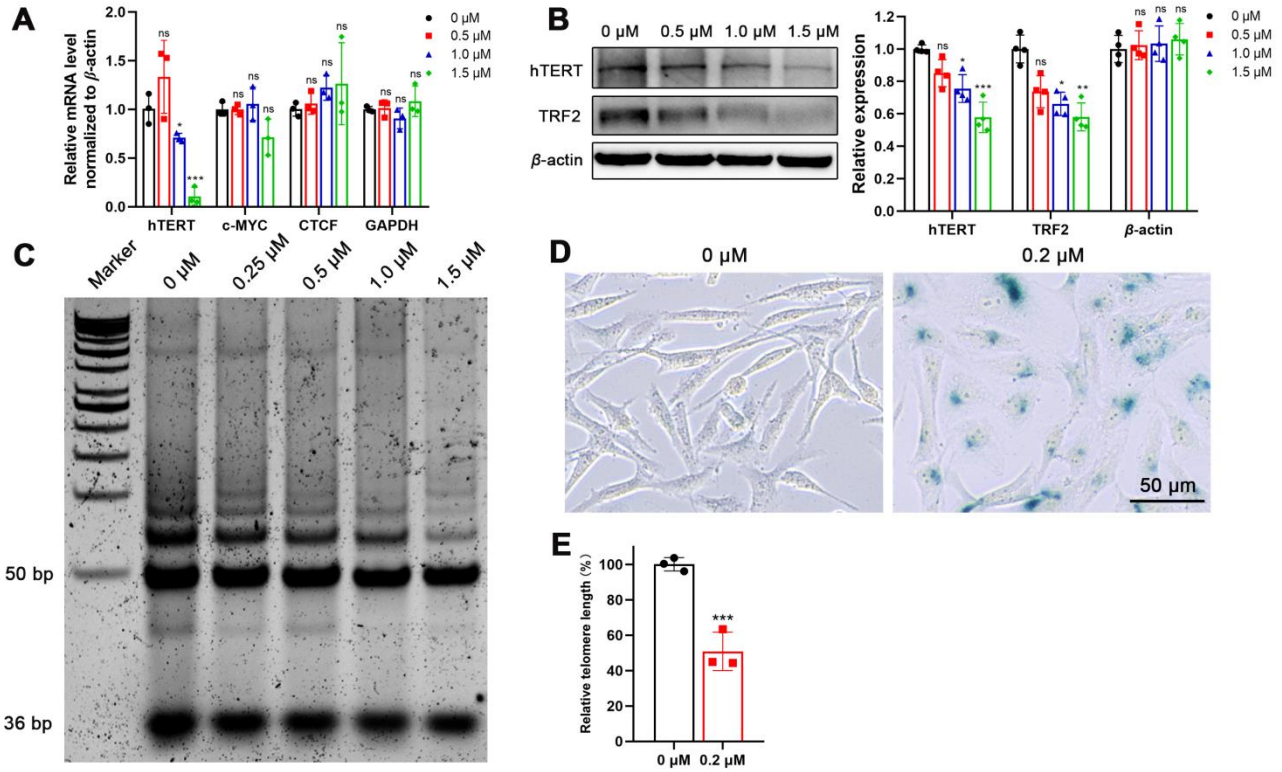

Figure 3. (A) The mRNA expression of *hTERT*, *c-MYC*, *CTCF*, *GAPDH* and *β-actin* genes in MDA-MB-231 cells treated with **5** (0–1.5 μM), respectively for 48 h and detected by real-time qRT-PCR. (B) Western Blot to determine the expression of hTERT, TRF2 and β-actin in MDA-MB-231 cells treated with **5** (0–1.5 μM) respectively for 48 h. (C) Concentration-dependent inhibition of telomerase activity by **5** (0–1.5 μM) in MDA-MB-231 cells. (D) The senescent effects caused by **5** (0.2 μM) treatment of MDA-MB-231 cells for ten days were detected using the SA-β-gal assay. (E) The results of relative telomere length measurement: MDA-MB-231 cells were treated with **5** (0.2 μM) for 10 days ((*) $P < 0.05$, (**) $P < 0.01$, and (***) $P < 0.001$, significantly different from the control; ns, not significantly different from the control).

2.5. Ligand 5 Induces DNA Damage, Senescence and Cell Cycle Arrest in MDA-MB-231 Cancer Cells. It has also been reported that the upstream promoter of the telomerase catalytic subunit *hTERT* gene not only acts as a master switch for regulating hTERT transcription and expression, but also regulates a variety of non-telomeric functions that are critically essential for cancer cell growth.[50] To gain insights into the effect of **5** on the noncanonical function of hTERT, Western Blot assays were applied to evaluate a number of DNA damage markers including cleaved PARP1, γ-H2AX and 53BP1 (Figure 4A and Figure S10) in MDA-MB-231 cells treated with **5**. We found that **5** at 0.5–1.5 μM significantly enhanced the expression levels of DNA damage signature proteins, 53BP1 and γ-H2AX,

indicating that **5** caused cellular DNA damage in a concentration dependent manner (Figure 4A). The upregulation of these markers indicates a cellular stress response to DNA damage induced by **5**.

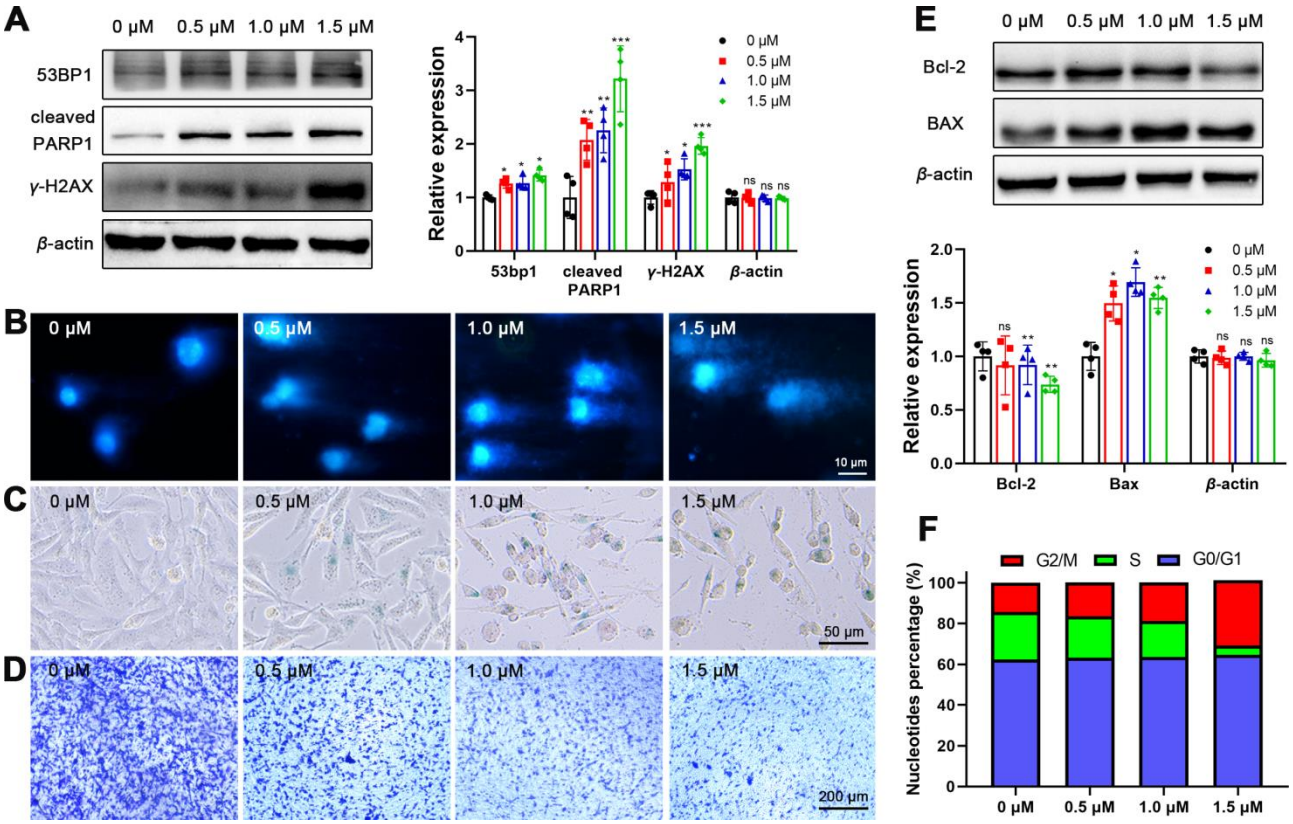

Figure 4. (A) Western Blot to determine the translation of 53BP1, cleaved-PARP1, *γ*-H2AX and *β*-actin in MDA-MB-231 cells treated with **5** (0–1.5 μM) respectively for 48 h. (B) Comet assay analysis of DNA damage in MDA-MB-231 cells after 48 h of treatment with **5** (0–1.5 μM). (C) The senescent effects caused by **5** (0–1.5 μM) treatment of MDA-MB-231 cells for 48 h were detected using the SA-*β*-gal assay. (D) Inhibitory effect of **5** (0–1.5 μM) on the migration of MDA-MB-231 cells after 48 h of treatment. (E) Western Blot to determine the translation of Bcl-2, BAX and *β*-actin in MDA-MB-231 cells treated with **5** (0–1.5 μM) for 48 h, respectively. (F) The cell cycle effects caused by **5** (0–1.5 μM) treatment of MDA-MB-231 cells for 48 h were detected using the flow cytometry. For all Western Blot experiments (N = 4, mean ± SD, (*) $P < 0.05$, (**) $P < 0.01$, and (***) $P < 0.001$, significantly different from the control; ns, not significantly different from the control).

In addition, from comet assays (Figure 4B), the cellular DNA fragmentation observed in the MDA-MB-231 cells treated with **5** (0.5–1.5 μM) was clearly higher than the untreated cells (control). These results indicate the **5**-treated cells under oxidative stress. The consequence of DNA damage and chromosomal instability is thus observed. Moreover, the DNA damage caused by **5** may induce senescence. Consequently, the ligand inhibited significantly the migration of MDA-MB-231 cells after the treatment for 48 h (Figure 4C,D). Furthermore, the apoptotic pathway of MDA-MB-231 cells was found activated (Figure 4E and Figure S11), in which the induced downregulation of anti-

apoptotic protein Bcl-2 and the upregulation of pro-apoptotic protein BAX in the MDA-MB-231 cells treated with **5** were observed in a concentration dependent manner (0.5–1.5 μM, 48 h).

Acute cellular senescence may also result in cell cycle perturbations such as cell cycle arrest or cell cycle deviation.[51] We found that, when MDA-MB-231 cells were treated with **5** (0.5–1.5 μM), the number of cells in G2/M phase was increased from 14.3% to 32% (Figure 4F and Figure S12). There were fewer cells in S phase (23.4%–4.6%). The cellular arrest in G2/M phase is likely attributed to DNA damage leading to the disruption of chromosome replication process.[52] Taken together, **5** may show effects on non-telomeric functions of hTERT in cancer cells, including a significant induction of DNA damage, acute cellular senescence, reduced capacity for cell migration, and cell cycle arrest.

2.6. Ligand 5 Inhibits Non-telomeric Functions of hTERT to Cause Mitochondrial Dysfunction and Disrupt Energy Metabolism in MDA-MB-231 Cells. It was reported that hTERT could be translocated from nucleus to mitochondria and bind to mitochondrial DNA to protect mitochondria from oxidative stress damage.[8] We thus investigated the effect of **5** on inhibiting the non-telomeric function of hTERT in mitochondrial functions when the expression of hTERT in MDA-MB-231 cells was downregulated with the ligand. TBHP (*tert*-butyl hydroperoxide), an inducer of oxidative stress commonly used in living cells,[53] showed an IC_{50} of 549 μM approximately in MDA-MB-231 cells for a 48-h treatment. When **5** was co-incubated with TBHP (200 μM) in the cells, the IC_{50} was found to be 0.67 μM, which was notably lower than the control (**5** alone, IC_{50} = 1 μM) (Figure S13).

From the results of immunofluorescence experiments (Figure 5A), hTERT (pink fluorescent foci) was predominantly located in the nuclear region of the untreated cells (control). However, in TBHP (200 μM) treatment group, a lot of pink foci were clearly observed in the cytoplasm of MDA-MB-231cells, indicating that hTERT was translocated from the nucleus to cytoplasm and then moving to mitochondria for repairing the mitochondria damaged by TBHP. For MDA-MB-231 cells treated with both **5** (0.5 μM) and TBHP (200 μM), the number of observable pink foci (hTERT) in both cytoplasm and nuclear region was clearly decreased. The results suggest that **5** may inhibit the expression of hTERT in the cells. Consequently, the effect of hTERT on maintaining mitochondrial functions may be suppressed with **5**, which is further investigated in the coming section.

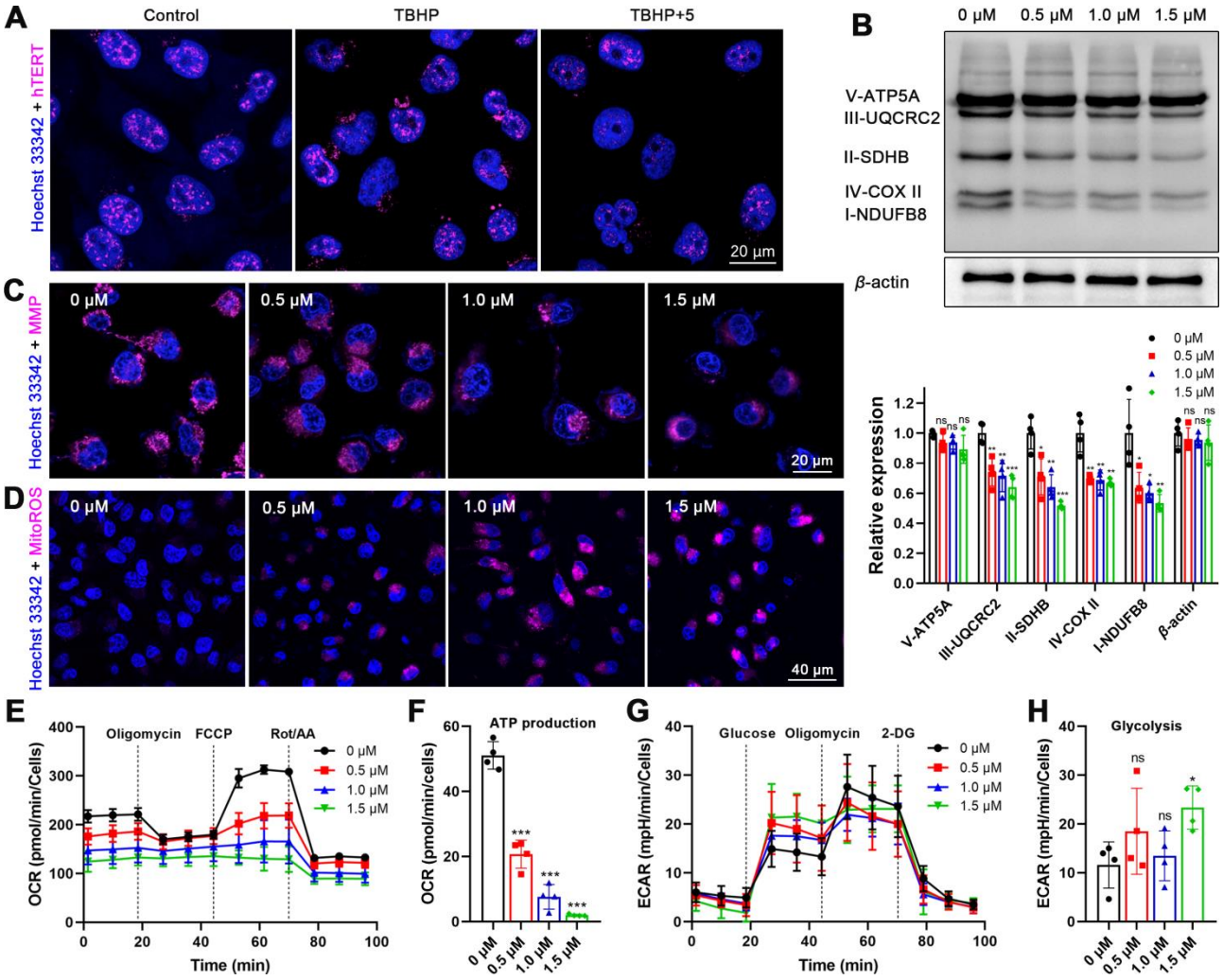

Figure 5. (A) MDA-MB-231 cells were treated with TBHP (200 μM) or a mixture of **5** (0.5 μM) and TBHP (200 μM) for 48 h and then analyzed for intracellular hTERT protein by immunofluorescence imaging. (B) Western Blot to determine the translation of mitochondria respiratory chain complex and β-actin in MDA-MB-231 cells treated with **5** (0–1.5 μM) respectively for 48 h. N = 4, mean ± SD, (*) $P < 0.05$, (**) $P < 0.01$, and (***) $P < 0.001$, significantly different from the control; ns, not significantly different from the control. (C) Mitochondrial Membrane potential (MMP) analysis in MDA-MB-231 cells after 48 h of treatment with **5** (0–1.5 μM). (D) Analysis of mitoROS production level in MDA-MB-231 cells after 48 h of treatment with **5** (0–1.5 μM). (E) Oxygen consumption rate of the **5**-treated cells in Mito Stress Test. (F) ATP production of the **5**-treated cells. (G) Proton efflux rate of the **5**-treated cells. (H) Induced glycolysis of the **5**-treated cells. For Seahorse experiment, N = 5, mean ± SD, (*) $P < 0.05$, (**) $P < 0.01$, and (***) $P < 0.001$, significantly different from the control; ns, not significantly different from the control.

To obtain more evidence to support that **5** caused mitochondrial dysfunctions in MDA-MB-231 cells, Western Blot assays were performed. The results showed that the mitochondrial respiratory chain complex (I–IV) was significantly downregulated in a concentration dependent manner in the **5**-treated cells (Figure 5B and Figure S14). We then further verified that the mitochondria of **5**-treated cells showed a markedly impaired mitochondrial membrane potential (MMP) (Figure 5C) and a markedly increased mitochondrial ROS (mitoROS) (Figure 5D). Furthermore, we evaluated the

effects of **5** on the oxygen consumption rate (OCR) and extracellular acidification rate (ECAR) because these two important indicators were closely related to cellular energy metabolism. The mito stress test and glycolytic rate test (Seahorse experiments) were also conducted for the MDA-MB-231 cells treated with **5**. The results (Figure 5E) showed that the OCR capacity of cells treated with **5** (1.5 μM) was significantly reduced compared to the untreated cells (control), indicating that **5** caused a decrease in cellular energy production. A similar trend is also observed in ATP production (Figure 5F), suggesting that **5** interrupts cellular energy production process. In addition, ECAR was found elevated (Figure 5G). The metabolic pathway of glycolysis was also significantly increased for more than 0.8-fold for the cells treated with **5** at 1.5 μM (Figure 5H). Taken together, these results demonstrate that **5** induces mitochondrial dysfunction and disrupts the energy metabolism in MDA-MB-231 cells. These cellular events observed could be caused by the downregulation of hTERT expression in **5**-treated MDA-MB-231 cells.

2.7. Ligand 5 Induces Mitochondrial Autophagy and Ferroptosis in MDA-MB-231 Cells. Since mitochondrial dysfunction is one of the important factors to induce cellular autophagy,[54] we thus evaluated the effect of **5** on the induction of mitochondrial autophagy in MDA-MB-231 cells. We examined the effect of autophagic vesicle formation in the cells treated with **5**. The live-cell confocal images (Figure 6A) clearly show that **5** induces mitochondrial phagocytosis. As increasing the concentration of **5** in the treatment, more autophagic vesicles (blue foci) were formed and observed in the cells. Then, the effect of **5** on autophagy protein markers was analyzed with Western Blot. BNIP3L/Nix is a selective substrate for mitochondrial autophagy (receptor-mediated) and p62 is one of the important substrates for PINK1/parkin-mediated mitochondrial autophagy (ubiquitin adapter-mediated).[55,56] The LC3 protein is also a key protein in autophagy process.[57] Thus, all these characteristic markers were investigated in MDA-MB-231 cells treated with **5**. The results showed that the expression of BNIP3L/Nix and LC3-II was significantly upregulated (Figure 6B and Figure S15). The overexpression of these proteins may promote the ability of cells to clear the damaged mitochondria to maintain cellular homeostasis.[58] Moreover, **5** at 1.5 μM significantly downregulated the expression of p62 and LC3-I, indicating that mitochondrial autophagy was attenuated or impaired.[59] Furthermore, from the lysosome-mitochondria co-localization study (Figure 6C), both lysosomes and mitochondria were found well-colocalized in MDA-MB-231 cells treated with **5**,

indicating that the damaged mitochondria were engulfed by lysosomes in the cells.

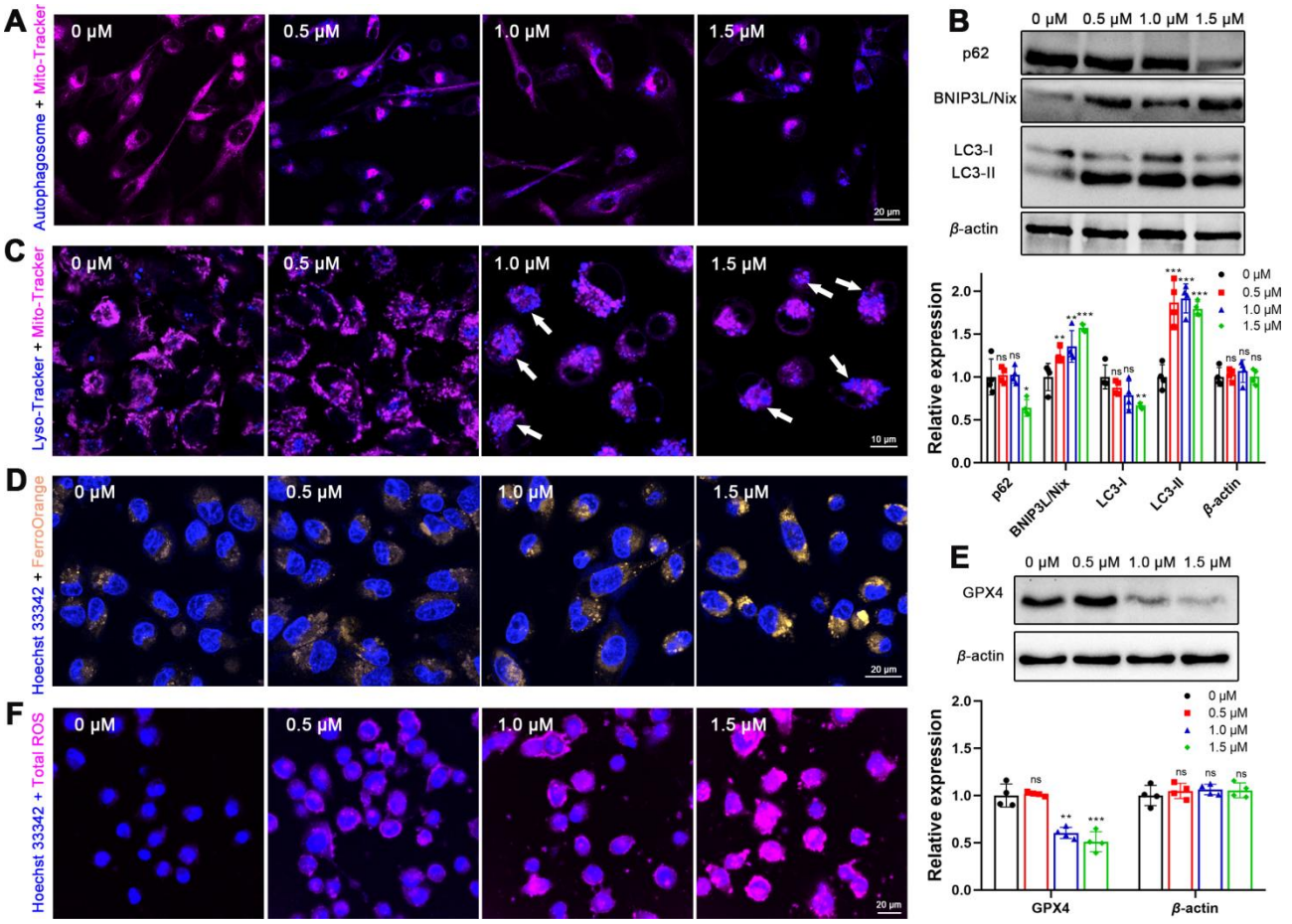

Figure 6. (A) **5** (0–1.5 μM) induced selective autophagy mitophagy in MDA-MB-231 cells. (B) Western Blot to determine the translation of p62, BNIP3L/Nix, LC3-I, LC3-II and *β*-actin in MDA-MB-231 cells treated with **5** (0–1.5 μM) respectively for 48 h. (C) **5** (0–1.5 μM) induces mitochondrial autophagy and delivers it to lysosomes for lysis. (D) Analysis of Fe^{2+} production level in MDA-MB-231 cells after 48 h of treatment with **5** (0–1.5 μM). (E) Western Blot to determine the translation of GPX4 and *β*-actin in MDA-MB-231 cells treated with **5** (0–1.5 μM) respectively for 48 h. (F) Analysis of total ROS production level in MDA-MB-231 cells after 48 h of treatment with **5** (0–1.5 μM). For all Western Blot experiments (N = 4, mean ± SD, (*) $P < 0.05$, (**) $P < 0.01$, and (***) $P < 0.001$, significantly different from the control; ns, not significantly different from the control).

It has been reported that there is a correlation between mitochondrial autophagy and ferroptosis.[60] We speculate that mitochondrial dysfunction caused by **5** may also result in abnormal iron metabolism, in which the excessive iron ions cause mitochondrial damage. We thus investigated the effect of **5** in ferroptosis in MDA-MB-231 cells. A commercial Fe(II) fluorescent sensing probe, FerroOrange, was utilized for assays. We observed that **5** induced a lot of bright yellow fluorescent spots (FerroOrange) in the cells and was found in a concentration dependent manner (Figure 6D). The results may support that **5** could disrupt the cellular iron metabolism and trigger ferroptosis in MDA-MB-231 cells.

Further Western Blot results (Figure 6E and Figure S16) also showed that **5** induced a significant decrease in glutathione peroxidase (GPX4) expression in the cells. The downregulation of GPX4 may cause an increase in the intracellular oxidative stress and exacerbated iron death.[61] In response to oxidative stress and iron metabolism disruption, the total cellular ROS production was found markedly increased in MDA-MB-231 cells treated with **5** in a concentration dependent manner (Figure 6F). Collectively, the results obtained suggest that **5** may downregulate hTERT expression, induce mitochondrial dysfunction and autophagy, and disrupt the iron metabolism to trigger ferroptosis in MDA-MB-231 cells.

2.8. mRNA Sequencing Analysis for MDA-MB-231 Cells Treated with Ligand 5. To further understand the anticancer mechanism of **5**, we performed mRNA sequencing (RNA-seq) analysis for MDA-MB-231 cells treated with **5** and DMSO (control). After filtering the standard of > 2.0-fold changes and a false discovery rate (FDR) < 0.05, a total of 2857 differentially expressed genes (DEGs) including 1174 upregulated genes and 1683 downregulated genes were screened in the **5**-treated cells compared to the control (Figure S17). Next, the screened DEGs were analyzed by Gene Ontology (GO) and Kyoto Encyclopedia of the Genome (KEGG) analyses to assess the effect of **5** on MDA-MB-231 cellular activity and function and to explore the potential activation pathways.

From the GO enrichment analysis, we found that DEGs were mainly enriched in biological processes, followed by cellular components and molecular functions, and all of them were markedly downregulated (Figure 7A). Among the above three gene-function classifications, we found that DEGs were mainly enriched in the key processes of cell proliferation such as chromosome segregation, DNA replication and cell cycle, indicating that **5** may play an antitumor role mainly by inhibiting cell proliferation (Figure 7A and Figure S18). In addition, we collated the GO enrichment related to telomere (Figure 7E), whose enrichment results indicated that **5** exhibited markedly negative effects on telomere maintenance and organization. The KEGG pathway enrichment also reveals the downregulation of DNA replication and cell cycle signaling pathways, similar to the results of GO enrichment analysis (Figure 7B). Furthermore, the KEGG pathway was enriched for a large number of apoptosis-related signaling pathways including calcium, TNF, FoxO, INF-1, JAK-STAT, necroptosis and cMAP signaling pathways. Moreover, all these signaling pathways were markedly upregulated, except TNF signaling pathway. We also found that the anti-apoptotic Hippo

signaling pathway and the promoting cell survival and proliferation Rap1 signaling pathways were downregulated. These results suggest that **5** may promote MDA-MB-231 cell apoptosis (Figure 7B). The upregulation of FoxO signaling pathway may trigger autophagy and promote apoptosis.[62]

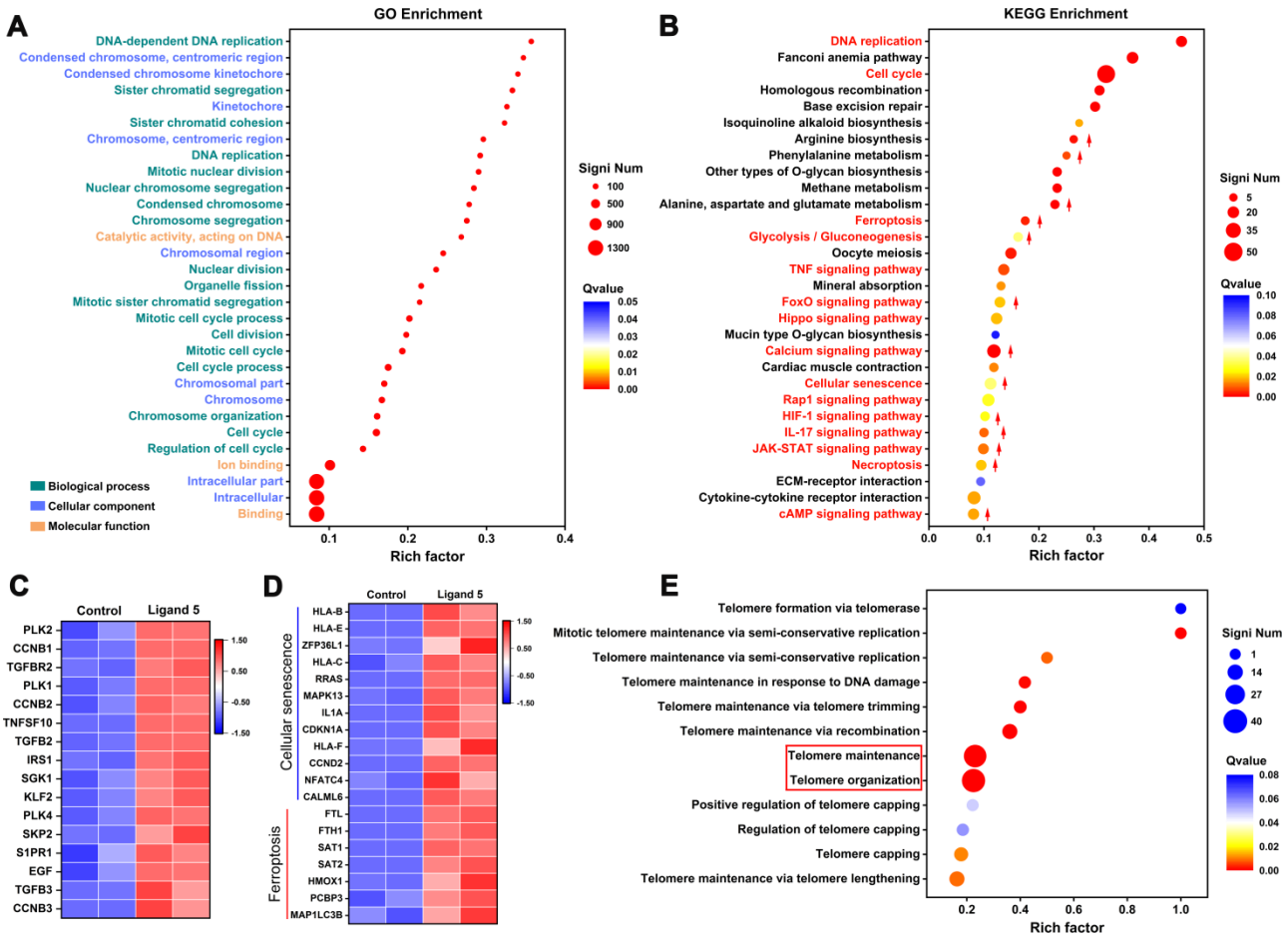

Figure 7. The analysis of enriched gene pathways of differentially expressed genes. Ligand **5** used for the assays was 1 μM. (A) GO enrichment analyses of differentially expressed genes between native and **5**-treated MDA-MB-231 cells. (B) KEGG pathway enrichment analysis of differentially expressed genes between native and **5**-treated MDA-MB-231 cells. (C) Heat map of differentially expressed genes related to autophagy in native and **5**-treated MDA-MB-231 cells (fold change > 2). (D) Heat map of differentially expressed genes related to cellular senescence and ferroptosis in native and **5**-treated MDA-MB-231 cells (fold change > 2). (E) GO enrichment analysis of differentially expressed genes on telomeres between native and **5**-treated MDA-MB-231 cells.

To compensate for the energy deficit, the glycolysis/glycolysis signaling pathway was also found upregulated in the cells treated with **5** probably because of the impaired mitochondrial function. The results suggest that **5** may induce mitochondrial dysfunction in MDA-MB-231 cells. Moreover, we found that the transcription levels of the key DNA repair genes *DNAPKcs* and *Artemis* in the non-homologous end-joining (NHEJ) signaling pathway were significantly downregulated in the **5**-treated cells (Figure S19), inducing DNA damage and oxidative stress.[63] Concomitantly, the oxidative

phosphorylation signaling pathway was markedly influenced (Figure S20) and the downregulation of ND1–ND6 expression, which are the components of mitochondrial NADH dehydrogenase complex (Complex I), resulted in mitochondrial dysfunction.[64] Subsequently, the FoxO signaling pathway was activated to trigger mitophagy, as demonstrated in the heatmap (more than 2-fold), the **5**-treated MDA-MB-231 cells increased the expression levels of 16 autophagy-related genes (Figure 7C). Moreover, the nuclear exported hTERT participates in antioxidant response to protect mtDNA, reduce mitoROS production, and improve mitochondrial functions.[65] **5** markedly inhibits hTERT expression at transcriptional level in the cells. The participation of hTERT in mitochondrial function is thus suppressed and then leads to mitochondrial dysfunction under oxidative stress and consequently, it affects cellular energy metabolism and activates the FoxO signaling pathway to trigger mitochondrial autophagy.

The results obtained from KEGG enrichment also reveals that the cellular senescence and ferroptosis signaling pathway are significantly upregulated. These findings suggest that **5** may disrupt cellular energy metabolism and trigger intracellular iron metabolism, and followed causing cellular senescence and ferroptosis. It is noteworthy that corresponding pathways enriched in 12 and 7 core genes associated with cellular senescence and iron metamorphosis were significantly upregulated (Figure 7D). All these bioinformatics indicate that **5** may disrupt cellular energy metabolism, trigger mitochondrial autophagy, induce cell cycle arrest and affect intracellular iron metabolism, and eventually it leads to cellular senescence and ferroptosis.

2.9. *In Vivo* Antitumor Activity of Ligand 5 in MDA-MB-231 Tumor-bearing Mice. All animal experiments performed in the present study were in compliance with the Animal Management Rules of the Ministry of Health of the People's Republic of China and were in compliance with the institutional ethics committee regulations and guidelines on animal welfare. The approved ASESC (Animal Subjects Ethics Sub-Committee) Case Number is 21-22/45-ABCT-R-GRF.

As **5** showed potent inhibitory effects on cancer cell growth, we further evaluated its antitumor activity in Balb/c-allogeneic MDA-MB-231 transplanted tumors. 18 female Balb/c nude mice bearing MDA-MB-231 tumors were randomly divided into three groups (6 mice per group), including control group (PBS), treatment group I (**5**, dose at 2 mg/kg) and treatment group II (**5**, dose at 5 mg/kg). The ligand was administered via tail vein injection. Throughout a 16-day treatment, no mice lost weight

significantly (Figure 8A) and all mice showed no signs of skin tears, ulcers, poor health, pain or discomfort. The results indicate that the treatment with **5** at the dose of 2 mg/kg and 5 mg/kg may be well-tolerated by mice. Moreover, the tumor growth was significantly inhibited by **5** in both treatment groups compared to the control group that showed fast-growing of tumors (Figure 8B). For treatment group I (**5**, 2 mg/kg), a reduction of 52.6% in tumor volume was achieved. The better result was found for treatment group II (**5**, 5 mg/kg) with 78.5% reduction of tumor volume. The mice were sacrificed on day 16 and the tumors were excised and weighed. The results showed a significant decrease in tumor weight after the treatment with **5**. The inhibition rates (weight %) of 48.7% (treatment group I, 2 mg/kg) and 78.7% (treatment group II, 5 mg/kg) were achieved, respectively (Figure 8C–E).

To further investigate the effect of **5** on tumor growth, histological images of H&E, TUNEL and Ki67 antigen immunofluorescence-stained tumor tissue sections were obtained (Figure 8F). It was found that the tumor tissues of the treatment group showed nuclear fragmentation and nucleolysis in H&E images in a concentration-dependent manner compared to the control group. For treatment group II (dose of 5 mg/kg), more severe apoptosis and necrosis was observed. Furthermore, both TUNEL and Ki67 staining assays clearly showed that **5** at the dose of 5 mg/kg exhibited stronger inhibitory effects on the proliferation of MDA-MB-231 tumor cells. These *in vivo* results suggest that **5** may show potent antitumor activity in Balb/c-xenogeneic MDA-MB-231 transplanted tumors.

For the evaluation of *in vivo* biocompatibility and cytotoxicity of **5**, whole blood was collected from mice at the end of the treatment cycle on day 16. The biochemical indices including liver function (ALT, AST, and ASP), blood urea nitrogen (BUN), renal function (creatinine (CREA) and uric acid (UA)), white blood cell count (WBC), lymphocyte count (Lymph), granulocyte count (Gran), red blood cell count (RBC), mean corpuscular volume (MCV), mean corpuscular hemoglobin concentration (MCHC), hemoglobin concentration (HGB), mean corpuscular hemoglobin (MCH) and platelet count (PLT) were assessed. The results (Figure 9A) confirmed that there was no significant change in the values of these indices between the treatment groups and the control group. We also evaluated H&E-stained sections of major organs including the heart, liver, spleen, lung and kidney in mice (Figure 9B). It was found that **5** (dose of 2 mg/kg and 5 mg/kg) did not produce pathological changes in any of these major organs. These results indicate that **5** may be highly compatible with normal tissues and shows no observable toxicity against the major organs examined.

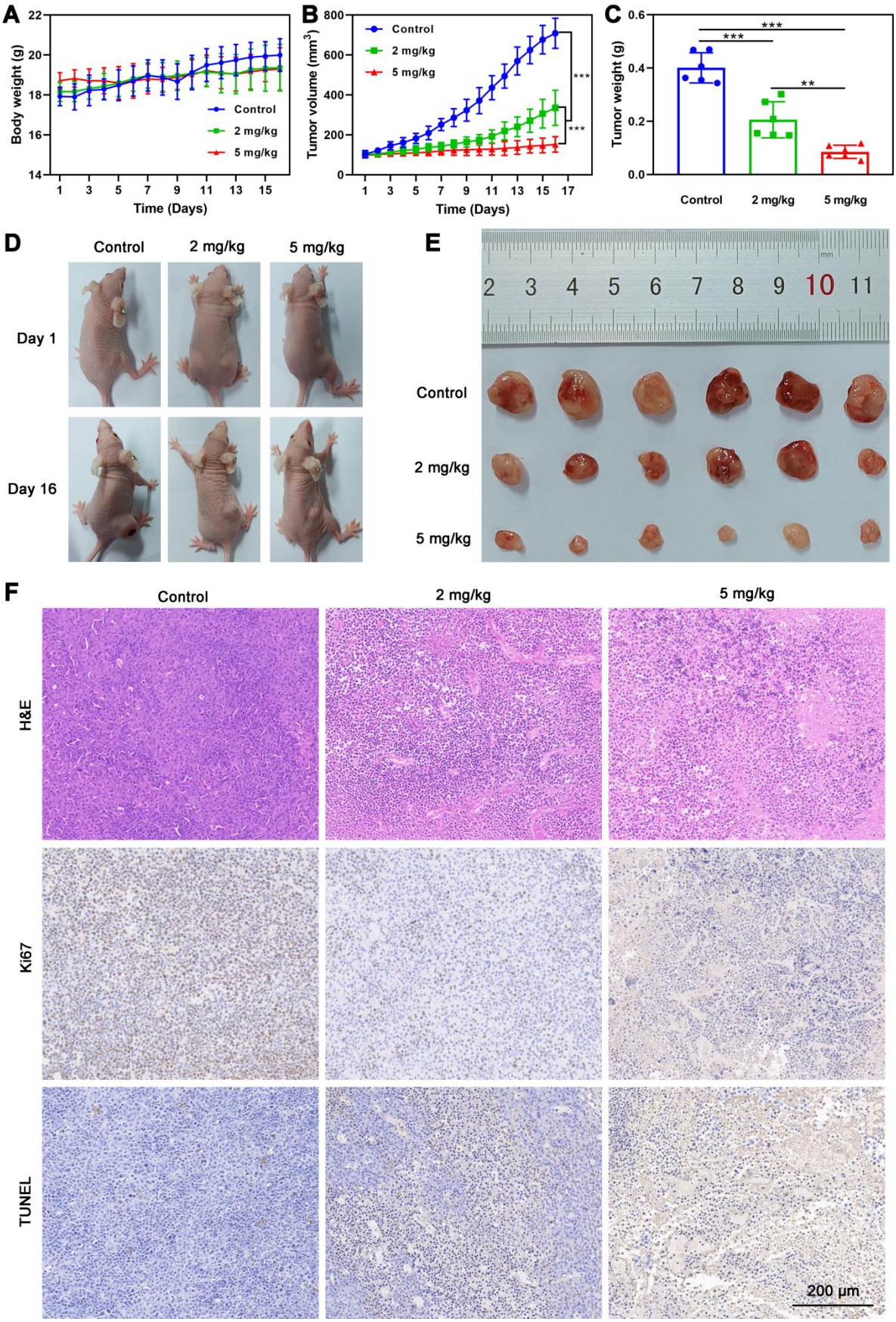

Figure 8. For *in vivo* experiments, 18 female Balb/c nude mice bearing MDA-MB-231 tumors were randomly divided into three groups (6 mice per group). (A) Body weight change of MDA-MB-231 tumor-bearing nude mice injected with **5** (2 mg/kg or 5 mg/kg) in tail vein for 16 days (N = 6, mean ± SD). Drug was administered every two days. (B) Time-dependent change of tumor volume after

different treatments for 16 days (N = 6, mean ± SD, (*) P < 0.05, (**) P < 0.01, and (***) P < 0.001, significantly different from the control; ns, not significantly different from the control). (C) Weight of isolated tumors in MDA-MB-231 tumor-bearing nude mice after 16 days of treatment (N = 6, mean ± SD, (*) P < 0.05, (**) P < 0.01, and (***) P < 0.001, significantly different from the control; ns, not significantly different from the control). (D) Digital photographs of MDA-MB-231 tumor-bearing nude mice on day 1 and day 16 of different groups. (E) Digital photographs of isolated tumors from different groups of MDA-MB-231-bearing nude mice after 16 days. (F) Representative histological images of H&E, TUNEL and Ki67 antigen immunofluorescence-stained tumor tissue sections of MDA-MB-231 tumor-bearing nude mice tumors from different groups after 16 days of treatment (Scale bars is 200 μm).

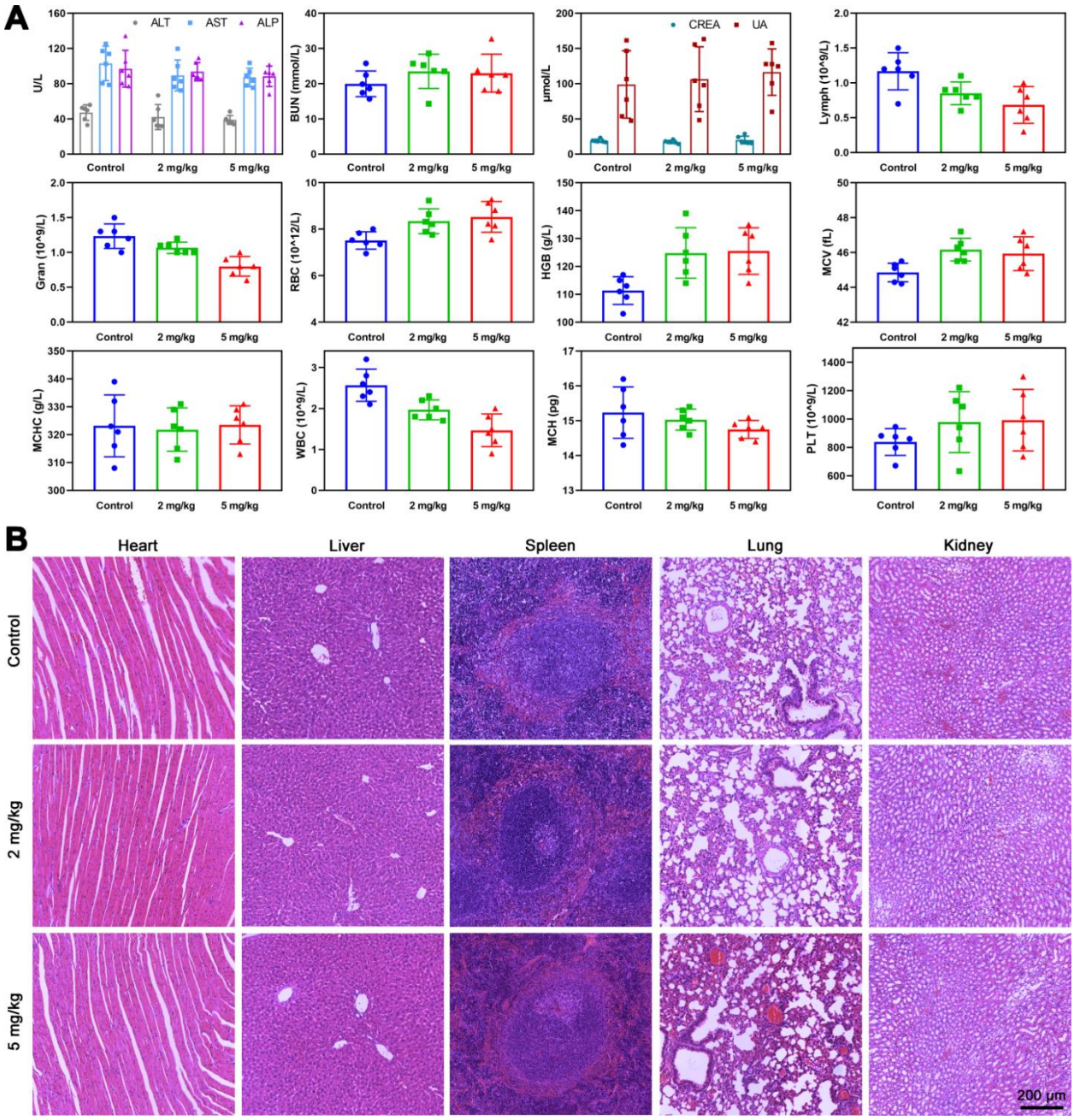

Figure 9. Effects on normal tissues and blood of nude mice after injection of **5**. (A) Blood biochemistry analysis of the ligands-treated mice 16 days post-injection under various conditions (N = 6, mean ± SD). (B) H&E-stained images of the major organs (heart, liver, spleen, lung, and kidney) from different groups (Scale bars is 200 μm).

3. CONCLUSION

In conclusion, a potent hTERT promoter G4-structure targeting small-molecule ligand capable of downregulating hTERT expression in triple-negative breast cancer cells (MDA-MB-231) was developed. Our results revealed that the ligand exhibited high affinity targeting hTERT G4-DNA (K_d = 1.1 μM). The ligand also showed potent anticancer activity against a broad range of human cancer cells (IC_{50} = 1–3.9 μM) including drug-resistant MDA-MB-231 cancer cells (IC_{50} = 1 μM). Moreover, we found that the ligand not only caused remarkable effects on canonical functions of hTERT including decreased telomerase activity, shortened telomere length and cellular senescence, but also induced important noncanonical functions including the induction of substantial DNA damage, acute cellular senescence and rapid apoptosis in MDA-MB-231 cells. In addition, our study demonstrated that the hTERT G4-DNA targeting ligand (**5**) was able to affect iron metabolism and activate ferroptosis in MDA-MB-231 cells. Based on the *in vitro* results obtained, it may suggest that hTERT G4-DNA could be a primary target of **5**. Nonetheless, it is noteworthy that the ligand causes rapid induction of diverse cellular responses in MDA-MB-231 cells, which may imply that the ligand could possibly influence multiple G4-related transcriptional events simultaneously *in cellulo* and *in vivo*. Furthermore, the *in vivo* antitumor efficacy of **5** was evaluated with an MDA-MB-231 xenograft mouse model. The mice treated with **5** (5 mg/kg, every 2-day, for 16-day) showed 78.7% reduction in tumor weight and no observable toxicity against the major organs was observed. The finding of the present study may provide new insights into the development of potent hTERT G4-DNA targeting small-molecule ligands for antitumor therapy via the inhibition of hTERT expression at transcriptional level, particularly the drug-resistant cancers such as triple-negative breast cancer.

4. EXPERIMENTAL SECTION

4.1. Synthesis and Characterization. High-resolution mass spectra (HRMS) were obtained by Agilent 1260-6230TOF. Using TMS as a reference, ^{1}H and ^{13}C NMR spectra were recorded at 400 MHz and 100 MHz in DMSO-d_6 with a Bruker BioSpin GmbH spectrometer. The high-performance liquid chromatography (HPLC) analysis for examining the purity of the compounds was performed on a SHIMADZU LC-16 system using a Diamonsil C18 column (250 × 4.6 mm, 5 μm) at room temperature with an elution using the mobile phase (MeOH/H_2O = 95:5 v/v). All ligands synthesized for assays were confirmed to have a purity ≥ 95%.

*4.1.1. General Procedures for the Synthesis of Ligands (**1**–**10**).* A synthetic route to ligands **1**−**10** is shown in Scheme 1. Intermediate **a** was obtained by the reaction using (1,2-dimethyl-4-[(3-bromopropyl-2(3H)-benzothiazolylidene)methyl]quinolinium iodide, 2.0 mmol) and 4-chloro-1,2-dimethylquinolin-1-ium iodide (2.0 mmol) for 24 h at 40 °C in cyclobutyl sulfone solution. Intermediate **b** was further obtained by reacting intermediate **a** (2.0 mmol) with 10.0 mmol of morpholine, diethylamine, piperidine, 4-(trimethyl-λ^4-fluoroamino)piperidine or 4-methylpiperidine for 24 h at 40 °C in methanol solution. The new ligands (**1**–**10**) were obtained by the reaction of **b** (1.0 mmol) and 1*H*-indole-3-carbaldehyde (2.0 mmol) or 1*H*-indole-2-carbaldehyde (2.0 mmol) and 4-methylpiperidine (200 μL), acetonitrile (10 mL) in 105 °C refluxed for 24 h. **1**–**10** obtained were purified by flash silica gel column chromatography and were confirmed with ^{1}H NMR, ^{13}C NMR, HRMS and HPLC (Figure S21–S30). The purity of all these isolated compounds determined by HPLC was 95% or higher.

*4.1.2. 2-((E)-2-(1H-indol-3-yl)vinyl)-1-methyl-4-((Z)-(3-(3-morpholinopropyl)benzo[d]thiazol-2(3H)-ylidene)methyl)quinolin-1-ium iodide (**1**).* Brownish red solid with an 76% ^{1}H NMR (600 MHz, DMSO-d_6) δ 12.02 (s, 1H), 8.63 (d, J = 8.3 Hz, 1H), 8.22 (s, 1H), 8.17 (d, J = 8.9 Hz, 2H), 8.04 – 7.96 (m, 3H), 7.75 – 7.69 (m, 3H), 7.56 (t, J = 8.1 Hz, 2H), 7.44 (d, J = 15.7 Hz, 1H), 7.36 (t, J = 7.5 Hz, 1H), 7.31 – 7.26 (m, 2H), 6.86 (s, 1H), 4.59 (t, J = 6.1 Hz, 2H), 4.19 (s, 3H), 3.49 (m, 4H), 2.40 (m, 2H), 2.26 (m, 4H), 2.02 – 1.97 (m, 2H). ^{13}C NMR (101 MHz, DMSO-d_6) δ 158.22, 154.01, 147.74, 141.03, 139.68, 137.97, 137.07, 133.49, 133.14, 128.33, 126.69, 125.48, 125.25, 124.30, 123.99 , 123.37, 121.74, 120.77, 119.06, 114.59, 114.10, 113.00, 108.06, 87.22, 66.55, 55.39, 53.80, 44.17, 38.33, 23.67. HRMS m/z: calcd for $C_{35}H_{35}N_4OS^+$ $[M-I]^+$ 559.25261; found 559.25220 $[M-I]^+$. HPLC analysis: retention time at 4.849 min eluted with MeOH/H_2O = 95:5 v/v, purity > 99%.

*4.1.3. 2-((E)-2-(1H-indol-3-yl)vinyl)-4-((Z)-(3-(3-(diethylamino)propyl)benzo[d]thiazol-2(3H)-ylidene)methyl)-1-methylquinolin-1-ium iodide (**2**).* Brownish red solid with an 62% ^{1}H NMR (400 MHz, DMSO-d_6) δ 12.03 (s, 1H), 8.75 (s, 1H), 8.28 (d, J = 2.3 Hz, 1H), 8.20 (dd, J = 16.1, 8.5 Hz, 2H), 8.08 – 8.05 (m, 1H), 8.00 (dd, J = 13.9, 6.5 Hz, 2H), 7.84 – 7.71 (m, 3H), 7.58 (dd, J = 16.9, 8.4 Hz, 2H), 7.48 (d, J = 15.7 Hz, 1H), 7.38 (t, J = 7.6 Hz, 1H), 7.32 – 7.25 (m, 2H), 6.87 (s, 1H), 4.65 (s, 2H), 4.24 (s, 3H), 3.16 (m, 4H), 2.41 (m, 2H), 2.16 (m, 2H), 1.23 (s, 6H). ^{13}C NMR (101 MHz, DMSO-d_6) δ 157.88, 154.25, 140.6

2, 139.70, 137.99, 133.51, 128.48, 126.72, 125.23, 124.42, 124.03, 123.51, 121.79, 120.82, 119.13, 114.47, 114.13, 113.11, 112.57, 47.05, 38.50, 9.22. HRMS m/z: calcd for $C_{35}H_{37}N_4S^+$ $[M-I]^+$ 545.27334; found 545.27142 $[M-I]^+$. HPLC analysis: retention time at 4.819 min eluted with MeOH/H_2O = 95:5 v/v, purity = 99.6%.

*4.1.4. 2-((E)-2-(1H-indol-3-yl)vinyl)-1-methyl-4-((Z)-(3-(3-(piperidin-1-yl)propyl)benzo[d]thiazol-2(3H)-ylidene)methyl)quinolin-1-ium iodide (**3**).* Brownish red solid with an 68% ^{1}H NMR (400 MHz, DMSO-d_6) δ 12.03 (s, 1H), 8.64 (s, 1H), 8.25 – 8.16 (m, 3H), 8.05 – 7.97 (m, 3H), 7.79 – 7.71 (m, 3H), 7.57 (dd, *J* = 16.3, 7.4 Hz, 2H), 7.48 (d, *J* = 15.7 Hz, 1H), 7.37 (t, *J* = 7.3 Hz, 1H), 7.32 – 7.26 (m, 2H), 6.87 (s, 1H), 4.61 (m, 2H), 4.22 (s, 3H), 2.48 – 2.10 (m, 6H), 2.00 (m, 2H), 1.39 (m, 6H). ^{13}C NMR (101 MHz, DMSO-d_6) δ 158. 15, 154.00, 147.76, 140.93, 139.66, 137.96, 137.09, 133.49, 133.17, 132.17, 131.99, 129.13, 128.31, 126.65, 125.49, 125.24, 124.31, 124.02, 123.96, 123.41, 123.36, 121.74, 120.76, 119 .04, 114.54, 114.09, 113.08, 112.81, 108.08, 87.13, 65.49, 54.31, 38.35, 30.48, 19.12, 14.02. HRMS m/z: calcd for $C_{36}H_{37}N_4S^+$ $[M-I]^+$ 557.27334; found 557.27277 $[M-I]^+$. HPLC analy sis: retention time at 4.831 min eluted with MeOH/H_2O = 95:5 v/v, purity > 99%.

*4.1.5. 2-((E)-2-(1H-indol-3-yl)vinyl)-1-methyl-4-((Z)-(3-(3-(4-methylpiperidin-1-yl)propyl)benzo[d]thiazol-2(3H)-ylidene)methyl)quinolin-1-ium iodide (**4**).* Brownish red solid with an 64% yi eld. ^{1}H NMR (400 MHz, DMSO-d_6) δ 12.01 (s, 1H), 8.60 (d, *J* = 8.1 Hz, 1H), 8.27 – 8.1 0 (m, 3H), 7.99 (dd, *J* = 23.4, 8.0 Hz, 3H), 7.70 (m, 3H), 7.55 (s, 2H), 7.44 (m, 1H), 7.3 3 (m, 3H), 6.85 (s, 1H), 4.56 (s, 2H), 4.18 (s, 3H), 2.71 (d, *J* = 10.1 Hz, 2H), 2.36 (s, 2 H), 1.98 (s, 2H), 1.79 (t, *J* = 10.7 Hz, 2H), 1.50 (d, *J* = 11.7 Hz, 2H), 1.23 (s, 1H), 1.04 (dd, *J* = 21.6, 10.5 Hz, 2H), 0.84 (d, *J* = 6.0 Hz, 3H). ^{13}C NMR (101 MHz, DMSO-d_6) δ 158.17, 153.90, 147.64, 140.94, 139.62, 137.95, 136.99, 133.45, 133.10, 128.29, 126.63, 1 25.29, 124.29, 123.96, 123.35, 121.75, 120.72, 118.97, 114.51, 114.06, 113.07, 112.85, 107. 94, 87.14, 55.21, 53.92, 44.26, 38.26, 34.32, 30.76, 24.19, 22.26. HRMS m/z: calcd for $C_{37}H_{39}N_4S^+$ $[M-I]^+$ 571.28899; found 571.28821 $[M-I]^+$. HPLC analysis: retention time at 4.833 min eluted with MeOH/H_2O = 95:5 v/v, purity > 99%.

*4.1.6. 2-((E)-2-(1H-indol-3-yl)vinyl)-1-methyl-4-((Z)-(3-(3-(4-(trifluoromethyl)piperidin-1-yl)propyl)benzo[d]thiazol-2(3H)-ylidene)methyl)quinolin-1-ium iodide (**5**).* Brownish red solid with an 70% yield. ^{1}H NMR (400 MHz, DMSO-d_6) δ 12.00 (s, 1H), 8.64 (d, *J* = 8.3 Hz, 1H),

8.21 – 8.15 (m, 3H), 8.00 (dt, *J* = 15.7, 7.3 Hz, 3H), 7.76 (s, 1H), 7.70 (m, 2H), 7.56 (t, *J* = 7.7 Hz, 2H), 7.46 (d, *J* = 15.7 Hz, 1H), 7.36 (t, *J* = 7.6 Hz, 1H), 7.31 – 7.26 (m, 2 H), 6.88 (s, 1H), 4.61 (t, *J* = 6.3 Hz, 2H), 4.20 (s, 3H), 2.81 (d, *J* = 10.9 Hz, 2H), 2.42 (s, 2H), 2.17 (s, 1H), 2.04 – 1.98 (m, 2H), 1.84 (t, *J* = 11.2 Hz, 2H), 1.68 (d, *J* = 11.8 Hz, 2H), 1.36 – 1.27 (m, 2H). ^{13}C NMR (101 MHz, DMSO-*d*$_6$) *δ* 158.23, 154.00, 147.77, 141.06, 139.69, 137.96, 137.02, 133.46, 133.06, 128.28, 126.63, 125.35, 124.30, 123.99, 123 .36, 121.72, 120.76, 119.06, 114.61, 114.09, 113.01, 108.03, 87.27, 54.91, 52.11, 44.24, 38. 33, 24.60, 24.10. HRMS m/z: calcd for $C_{37}H_{36}F_3N_4S^+$ [M-I]$^+$ 625.26073; found 625.26001 [M-I]$^+$. HPLC analysis: retention time at 4.851 min eluted with MeOH/H_2O = 95:5 v/v, puri ty = 98.1%.

*4.1.7. 2-((E)-2-(1H-indol-2-yl)vinyl)-1-methyl-4-((Z)-(3-(3-morpholinopropyl)benzo[d]thiazol-2 (3H)-ylidene)methyl)quinolin-1-ium iodide (**6**)*. Brownish red solid with an 67% yield. ^{1}H N MR (400 MHz, DMSO-*d*$_6$) *δ* 11.86 (s, 1H), 8.68 (d, *J* = 6.7 Hz, 1H), 8.18 (d, *J* = 8.7 Hz , 1H), 8.07 (d, *J* = 7.7 Hz, 1H), 8.00 (t, *J* = 7.3 Hz, 1H), 7.80 – 7.68 (m, 5H), 7.64 (d, *J* = 7.9 Hz, 1H), 7.59 (t, *J* = 7.7 Hz, 1H), 7.49 (d, *J* = 8.2 Hz, 1H), 7.40 (t, *J* = 7.4 Hz , 1H), 7.26 (t, *J* = 7.5 Hz, 1H), 7.09 (m, 2H), 6.92 (s, 1H), 4.65 (m, 2H), 4.19 (s, 3H), 3 .49 (m, 4H), 2.39 (m, 2H), 2.25 (m, 4H), 2.01 (m, 2H). ^{13}C NMR (101 MHz, DMSO-*d*$_6$) *δ* 159.09, 152.06, 148.04, 140.94, 139.69, 138.77, 135.59, 133.65, 131.99, 131.84, 129.13, 1 28.46, 126.95, 125.50, 124.80, 124.62, 124.20, 124.01, 123.37, 121.70, 120.50, 119.09, 113. 26, 111.97, 109.45, 107.97, 87.83, 66.52, 65.50, 55.37, 53.78, 44.35, 38.33, 30.47, 23.73, 1 9.12, 14.02. HRMS m/z: calcd for $C_{35}H_{35}N_4OS^+$ [M-I]$^+$ 559.25261; found 559.25238 [M-I]$^+$. HPLC analysis: retention time at 4.785 min eluted with MeOH/H_2O = 95:5 v/v, purity = 9 7.1%.

*4.1.8. 2-((E)-2-(1H-indol-2-yl)vinyl)-4-((Z)-(3-(3-(diethylamino)propyl)benzo[d]thiazol-2(3H)-yl idene)methyl)-1-methylquinolin-1-ium iodide (**7**)*. Brownish red solid with an 59% yield. ^{1}H NMR (400 MHz, DMSO-*d*$_6$) *δ* 11.87 (s, 1H), 8.74 (s, 1H), 8.22 (d, *J* = 8.7 Hz, 1H), 8.09 (d, *J* = 7.7 Hz, 1H), 8.05 – 7.99 (m, 1H), 7.87 – 7.68 (m, 5H), 7.63 (dd, *J* = 16.2, 7.8 Hz, 2H), 7.49 (d, *J* = 7.7 Hz, 1H), 7.43 (d, *J* = 7.2 Hz, 1H), 7.27 (t, *J* = 7.6 Hz, 1H), 7 .15 (s, 1H), 7.08 (t, *J* = 7.9 Hz, 1H), 6.93 (s, 1H), 4.75 – 4.57 (m, 2H), 4.22 (s, 3H), 3.1 0 (m, 4H), 2.11 (m, 4H), 1.17 (m, 6H). ^{13}C NMR (101 MHz, DMSO-*d*$_6$) *δ* 158.22, 151.66,

147.74, 139.96, 139.09, 138.21, 135.04, 133.15, 131.50, 128.55, 127.92, 126.40, 124.18, 123.58, 123.01, 121.14, 119.93, 118.53, 112.33, 111.40, 108.97, 107.74, 87.10, 64.91, 46.40, 37.93, 29.90, 18.54, 13.44. HRMS m/z: calcd for $C_{35}H_{35}N_4OS^+$ $[M-I]^+$ 559.25261; found 559.25238 $[M-I]^+$. HPLC analysis: retention time at 4.821 min eluted with MeOH/H_2O = 95:5 v/v, purity = 96.1%.

*4.1.9. 2-((E)-2-(1H-indol-2-yl)vinyl)-1-methyl-4-((Z)-(3-(3-(piperidin-1-yl)propyl)benzo[d]thiazol-2(3H)-ylidene)methyl)quinolin-1-ium iodide (**8**).* Brownish red solid with an 62% yield. ^{1}H NMR (400 MHz, DMSO-d_6) δ 11.86 (s, 1H), 8.69 (s, 1H), 8.20 (d, J = 7.7 Hz, 1H), 8.07 (d, J = 7.7 Hz, 1H), 8.01 (t, J = 7.0 Hz, 1H), 7.81 – 7.71 (m, 5H), 7.65 (d, J = 7.9 Hz, 1H), 7.61 (t, J = 7.5 Hz, 1H), 7.49 (d, J = 8.1 Hz, 1H), 7.41 (t, J = 7.5 Hz, 1H), 7.27 (t, J = 7.6 Hz, 1H), 7.10 (m, 2H), 6.92 (s, 1H), 4.65 (s, 2H), 4.21 (s, 3H), 2.49 – 2.07 (m, 6H), 2.01 (m, 2H), 1.39 (m, 6H). ^{13}C NMR (101 MHz, DMSO-d_6) δ 158.38, 151.57, 147.69, 140.01, 139.07, 138.21, 135.58, 135.09, 133.07, 131.41, 128.55, 127.86, 124.10, 123.57, 122.94, 121.10, 119.88, 118.53, 112.45, 111.41, 108.76, 107.61, 87.12, 64.91, 47.31, 37.89, 29.89, 18.54, 13.43. HRMS m/z: calcd for $C_{36}H_{37}N_4S^+$ $[M-I]^+$ 557.27334; found 557.27289 $[M-I]^+$. HPLC analysis: retention time at 4.835 min eluted with MeOH/H_2O = 95:5 v/v, purity > 99%.

*4.1.10. 2-((E)-2-(1H-indol-2-yl)vinyl)-1-methyl-4-((Z)-(3-(3-(4-methylpiperidin-1-yl)propyl)benzo[d]thiazol-2(3H)-ylidene)methyl)quinolin-1-ium iodide (**9**).* Brownish red solid with an 67% yield. ^{1}H NMR (400 MHz, DMSO-d_6) δ 11.84 (s, 1H), 8.64 (d, J = 8.3 Hz, 1H), 8.17 (d, J = 8.8 Hz, 1H), 8.06 (d, J = 7.8 Hz, 1H), 8.00 (t, J = 7.8 Hz, 1H), 7.83 – 7.67 (m, 5H), 7.66 – 7.63 (m, 1H), 7.58 (t, J = 7.8 Hz, 1H), 7.48 (d, J = 8.2 Hz, 1H), 7.40 (t, J = 7.6 Hz, 1H), 7.26 (t, J = 7.3 Hz, 1H), 7.12 – 7.05 (m, 2H), 6.92 (s, 1H), 4.62 (t, J = 6.4 Hz, 2H), 4.18 (s, 3H), 2.71 (d, J = 10.7 Hz, 2H), 2.35 (m, 2H), 2.04 – 1.95 (m, 2H), 1.79 (t, J = 9.4 Hz, 2H), 1.49 (m, 2H), 1.23 (s, 1H), 1.03 (m, 2H), 0.84 (d, J = 6.5 Hz, 3H). ^{13}C NMR (101 MHz, DMSO-d_6) δ 158.51, 151.40, 147.40, 140.32, 139.09 , 138.19, 135.01, 133.03, 131.21, 127.84, 126.32, 124.90, 124.12, 123.65, 123.42, 122.79, 121.11, 119.92, 118.49, 112.63, 111.38, 108.86, 107.33, 87.24, 54.63, 53.35, 43.87, 37.74, 33.77, 30.19, 23.72, 21.69, 13.74. HRMS m/z: calcd for $C_{36}H_{37}N_4S^+$ $[M-I]^+$ 557.27334; found 557.27289 [

M-I]$^+$. HPLC analysis: retention time at 4.839 min eluted with MeOH/H_2O = 95:5 v/v, puri ty > 99%.

*4.1.11. 2-((E)-2-(1H-indol-2-yl)vinyl)-1-methyl-4-((Z)-(3-(3-(4-(trifluoromethyl)piperidin-1-yl)p ropyl)benzo[d]thiazol-2(3H)-ylidene)methyl)quinolin-1-ium iodide (**10**).* Brownish red solid wit h an 63% yield. ^{1}H NMR (600 MHz, DMSO-d_6) δ 11.86 (s, 1H), 8.68 (d, J = 8.1 Hz, 1H), 8.18 (d, J = 8.7 Hz, 1H), 8.06 (d, J = 7.9 Hz, 1H), 8.00 (t, J = 7.7 Hz, 1H), 7.74 (m, 6H), 7.64 (d, J = 7.9 Hz, 1H), 7.58 (d, J = 7.8 Hz, 1H), 7.48 (d, J = 8.1 Hz, 1H), 7.40 (d, J = 7.5 Hz, 1H), 7.26 (d, J = 7.4 Hz, 1H), 7.10 – 7.07 (m, 2H), 4.65 (t, J = 6.1 Hz, 2H), 4.19 (s, 3H), 2.79 (m, 2H), 2.41 (m, 2H), 2.18 (s, 1H), 2.01 (m, 2H), 1.83 (m, 2H), 1.67 (m, 2H), 1.30 (m, 2H). ^{13}C NMR (101 MHz, DMSO-d_6) δ 158.54, 151.47, 147.49, 14 0.39, 139.12, 138.20, 135.01, 133.05, 131.23, 129.53, 127.84, 126.31, 124.90, 124.14, 123.5 3, 122.77, 121.13, 119.93, 118.54, 112.70, 111.39, 108.87, 107.37, 87.31, 54.32, 51.52, 43.8 5, 37.74, 28.91, 28.46, 24.00, 23.58, 13.83. HRMS m/z: calcd for $C_{37}H_{36}F_3N_4S^+$ [M-I]$^+$ 625. 26073; found 625.26019 [M-I]$^+$. HPLC analysis: retention time at 4.830 min eluted with M eOH/H_2O = 95:5 v/v, purity > 99%.

5. MATERIALS AND METHODS

5.1. UV-visible and Fluorescence Assays. The UV-vis spectrum was obtained by using the UV-2600i Spectrophotometer (SHIMADZU), ligand **5** (5 μM) were dissolved in Tris-HCl buffer (10 mM, pH 7.4) containing 60 mM KCl, and nucleic acids (hTERT, 0–10 μM) were added slowly. The fluorescence spectrum was recorded on the FLS 1000 fluorescence spectrometer (Edinburgh), the colorimetric dish has a slit width of 1 mm and an optical diameter of 10 mm, compounds (5 μM) were dissolved in Tris-HCl buffer (10 mM, pH 7.4) containing 60 mM KCl, and different nucleic acids (double stranded, single stranded, G4-DNA) were added slowly until the titration was saturated. Resulting data were analyzed using Origin 2019. All oligonucleotides used in this work were synthesized and purified by Shanghai Sangon Biotechnology Co., Ltd. (Shanghai, China), and their sequences were listed in (Table S1).

5.2. Circular Dichroism (CD). The CD spectrum was measured by JASCO J-1500 Circular Dichroism Spectrometer (JASCO). DNA sequences (Table S1) were pre-annealed in 10 mM Tris-HCl Buffer (containing 20 mM KCl, pH = 7.4) by heated to 95 °C in water bath for 5 min and then

cooled to room temperature. The concentration of ligand **5** is 0–10 times that of the DNA substrates, using a quartz cuvette with a path length of 1 mm to record the spectral data in the wavelength range of 220–700 nm with a bandwidth of 1 nm, a step of 1 nm and a point of 0.5 s/point, the CD spectral data are obtained by averaging three scans. In addition, for the CD melting experiment, 10 μM concentration of DNA substrates were prepared with 10 mM Tris-HCl buffer (containing 20 mM KCl, pH = 7.4) and ligand **5** was added to the mixture for CD melting. Data were recorded at 1 °C intervals in the range 25–95 °C at a heating rate of 1.0 °C /min. Final data analysis was performed using Origin 2019.

5.3. Isothermal Titration Calorimetry (ITC). ITC experiments were performed using the MicroCal PEAQ-ITC microcalorimeter (Malvern). DNA sequences were pre-annealed in 25 mM KH_2PO_4, 60 mM KCl buffer (pH 7.4, containing 1% (v/v) DMSO and 0.5% (v/v) Twain20) by heated to 95 °C in water bath for 5 min and then cooled to room temperature. The pre-annealed DNA sequence (10 μM, Table S1) in buffer was kept in the sample cell and ligand **5** (400 μM) were filled in the syringe of a volume 40 μl in the same buffer. Ligand **5** were mixed with the samples at 25 °C in a stirring syringe, with a speed of 750 rpm, undergoing 25 injections. Ligand **5** was injected 0.4 μL for the first injection and 2 μL for each of the remaining injections, with a duration of 4 s for each injection and an equilibrium time of 150 s. MicroCal PEAQ-ITC analysis software was used to analyze the ITC data.

5.4. ^{1}H NMR Titration Study. The oligomeric DNA (Table S1) solution at 160 μM was prepared with phosphate buffer (25 mM KH_2PO_4, 10% D_2O, 20 mM KCl, pH = 7.4), heated to 95 °C, allowed to equilibrate to room temperature and incubated for 24 h. During the measurement, the ligand **5** was gradually added to the DNA solution with a concentration range of 160–480 μM for NMR analysis. Experiments were performed at 25 °C on a 600 MHz spectrometer (Bruker).

5.5. Cell Lines and Cell Culture. The cell lines including A549 (CCL-185), HeLa (CRM-CCL-2), PC3 (CRL-1435), HepG2 (HB-8065), MDA-MB-231 (HTB-26), U2OS (HTB-96), HUEVC (PCS-100-013) and HK-2 (CRL-2190) were purchased from ATCC. The cell lines were cultured in different complete medium as shown below: HeLa, HepG2, MDA-MB-231 and HK2 were cultured in DMEM (Gibco) supplemented with 10% fetal bovine serum (FBS) (Gibco) and 1% P/S (Gibco). A549, PC3, HUEVC were cultured in F-12K (Gibco) supplemented 10% FBS and 1% P/S. U2OS was cultured in McCoy's 5A (Gibco) supplemented with 10% FBS and 1% P/S. The cells were incubated in incubator at 37 °C with 5% CO_2.

5.6. Fluorescence Microscopy Imaging Study and Staining Effects. Fluorescence microscopy images of MDA-MB-231 cells were captured using a confocal laser scanning microscope (ZEISS LSM 900 with Airscan). The reference dye used for nucleus localization was Hoechst 33342. The dye was excited at a wavelength of 405 nm and its emission was collected within the range of 420–500 nm. Ligand **5** was excited using a wavelength of 488 nm and its emission was collected within the range of 500–630 nm. At a concentration of 5 μM of ligand **5**, the compounds entered the cells rapidly without disrupting cellular activity.

5.7. Cell Imaging of MDA-MB-231 Cells Treated with RNase and DNase. MDA-MB-231 cells were cultured in confocal dishes for 24 h. Before staining experiments, cells were fixed with pre-cooled paraformaldehyde for 5 min, washed three times with PBS and then treated with 1% Triton X-100 for 15 min to permeabilize the cell membrane, and continued to be washed three times with PBS. Pretreated MDA-MB-231 cells were stained with ligand **5** at 25 °C for 10 min, and after sufficient washing with PBS, stained with Hoechst 33342 for 10 min. After being washed with PBS, cell was treated with 200 units/mL RNase (Thermofisher Scientific) or DNase (Sigma) at 37 °C for 2 h. Imaging experiments were performed on a Zeiss LSM900 confocal laser scanning microscope (ligand **5**, λ_{ex} = 488 nm, λ_{em} = 500–630 nm; Hoechst 33342, λ_{ex} = 405 nm, λ_{em} = 420–500 nm). Finally, the data were collected and analyzed.

5.8. BG4 Immunofluorescence Experiments in MDA-MB-231 Cells. MDA-MB-231 cells were incubated with ligand **5** (5 μM) for 2 h and then fixed with 4% paraformaldehyde for 20 min, followed by permeabilization with 0.1% Triton-X 100/PBS for 30 min at 37 °C and infiltrated with 1% BSA/PBS for 1 h at 37 °C. Immunofluorescence assays were performed using standard methods, first incubated with anti-DNA G-quadruplex antibody BG4 (MABE917, Merck Millipore) for 3 h at 37 °C, washed 6 times with 1% BSA/PBS and then incubated with DYKDDDDK Tag Antibody (Cell signaling technology, #2368) for 1 h at 37 °C and washed 6 times with 1% BSA/PBS. Finally, incubated with Alexa Fluor 647 goat anti-rabbit lgG (H+L) (Thermo Fisher Scientific, A21235) for 1 h at 37 °C and washed 6 times with 1% BSA/PBS. Digital images were recorded with a Zeiss LSM 900 microscope (ligand **5**, λ_{ex} = 488 nm, λ_{em} = 500–630 nm; Alexa Fluor 647 goat anti-rabbit lgG (H+L), λ_{ex} = 640 nm, λ_{em} = 660–700 nm) and analyzed using ZEN software.

5.9. Cytotoxicity and Cell Migration Studies. For cytotoxicity studies, cancer cells such as MDA-MB-231 and normal cells were inoculated in 96-well plates, and after the cells were cultured to the

logarithmic growth phase, the cells were incubated with different concentrations of ligands **1**–**10** for 48 h, and then the cell viability was detected by the standard MTT method. For cell migration studies, MDA-MB-231 cells were cultured in the upper chamber of transwell 24-well plates, complete medium was added to the bottom chamber of transwell 24-well plates, and cells were incubated with different concentrations of ligand **5** for 48 h. Then, carefully wipe off the cells on the surface of the upper chamber polycarbonate membrane with a cotton swab, fix the upper chamber with methanol for 30 min, then stain with 1% crystal violet for 10 min, wash thoroughly with PBS, and observe under a microscope to analyze the effect of ligand **5** on the migration of MDA-MB-231 cells.

5.10. Telomerase Activity Assays. Telomerase activity was determined using the TRAPeze Telomerase Detection Kit (S7700, Sigma-Aldrich). Briefly, 1×10^6 cells were resuspended in 200 μL of CHAPS lysis buffer and incubated on ice for 30 min according to the manufacturer's instructions. Cells were centrifuged at 4 °C for 20 min and the supernatant was collected in sterile, enzyme-free tubes, and protein concentration was determined using a BCA Kit (P0010, Beyotime Biotechnology). Each 50 μl reaction mixture contained 5 μL of 10×TRAP Reaction Buffer, 1 μL of 50×dNTP Mix, 2 μL of TS Primer, 1.0 μL of TRAP Primer Mix, 2 Units of Taq Polymerase (Sigma-Aldrich), ddH_2O and 200 ng of extracted protein. The reaction mixture was incubated in a thermocycler at 30 °C for 30 min. telomerase products were amplified by PCR (34 cycles of 94 °C for 15 s, 59 °C for 30 s, and 72 °C for 1 min), and at the end of the amplification the PCR products were separated by electrophoresis in a 10% non-denaturing polyacrylamide gel. After electrophoresis, the products were stained with SYBR Gold for 30 min at room temperature and photographed to collect the imaging data.

5.11. Relative Telomere Length Determination. MDA-MB-231 cells were treated with different concentrations of ligand **5** for 10 days, after digestion the cells were centrifuged, followed by washing the cells 2 times with PBS solution, centrifugation and careful pouring off of the PBS. The gDNA was isolated by utilizing a DNA extraction kit (KIT0103, Thermo Fisher Scientific) and quantified by Nanodrop UV-Vis spectrophotometer (Thermofisher Scientific). 1-10 ng of gDNA, the 2×Maxima SYBR Green qPCR Master Mix (K0251, Thermofisher Scientific), ROX solution (K0251, Thermofisher Scientific), nuclease-free water and associated primer sequences (Table S2) were used for relative telomere length determination. The qRT-PCR method was used to amplify the gDNA (step 1: 1 cycle, 50 °C for 2 min, step 2: 1 cycle, 95 °C for 10 min, step 3: 40 cycles, 95 °C for 15 s,

60 °C for 30 s, and 72 °C for 30 s). All experiments were repeated three times and DNA expression levels were normalized using the housekeeping gene hRPLPO. Amplified DNA was measured by the Ct ($\Delta\Delta$CT) method to estimate relative telomere length.

5.12. β-Galactosidase (SA-β-gal) Staining of Cell Senescence. MAD-MB-231 cells were inoculated in a six-well plate at a density of 1×10^6 cells/well. After overnight incubation, cells were treated with different concentrations of ligand 5 for 48 h or 10 days. For prolonged incubation experiments, the medium was replaced every three days, and to avoid excess cells in the control group over a long period of time, the control group was passaged every three days. At the end of the incubation time senescence staining assay was performed using β-galactosidase senescence assay kit (C0602, Beyotime Biotechnology). Firstly, the medium was removed, and the β-galactosidase staining fixative was added after sufficiently washed with PBS and fixed for 15 min at room temperature. Then the cell fixative was taken out, and the working solution for β-galactosidase staining was added after sufficiently washed with PBS and incubated overnight at 37 °C. The cells were then stained with the β-galactosidase staining fixative for 15 min at room temperature. Finally, the cells were observed and data were collected under an inverted microscope (Olympus CKX53).

5.13. RNA Isolation and qRT-PCR. MAD-MB-231 cells were inoculated into six-well plates at a density of 1×10^6 cells/well, and after overnight incubation, the cells were treated with different concentrations of ligand **5** for 48 h. RNA was extracted using the RNase Mini Kit (74106, Qiagen), and RNA samples were prepared according to the manufacturer's instructions. The RNA samples were then treated with the DNA-free DNA removal kit (Thermofisher Scientific) to remove DNA. The RNA samples were quantified using a Nanodrop UV-Vis spectrophotometer (Thermofisher Scientific). The QuantStudio Flex Real-Time PCR System (Applied Biosystems) was used for reverse transcription of RNA and DNA amplification experiments. 0.5-2 µg of RNA, BeyoFast SYBR Green One-Step qRT-PCR Kit (D7268M, Beyotime Biotechnology), nuclease-free water and the relevant primer sequences (Table S3) were used for reverse transcription of RNA and amplification of DNA. qRT-PCR conditions were as follows: one cycle of 50 °C for 30 min, one cycle of 95 °C for 2 min, followed by 40 cycles of 95 °C for 15 s, 60 °C for 30 s and 72 °C for 30 s. All experiments were repeated thrice and gene expression levels were normalized using the housekeeping gene β-actin. The Ct ($\Delta\Delta$CT) method was utilized to compare the mRNA expression levels of the genes of interest.

5.14. Western Blot Assay. MDA-MB-231 cells in logarithmic growth phase were treated with different concentration gradients of ligand **5** for 48 h. Cells were collected by centrifugation and incubated with RIPA buffer on ice for 30 min, then centrifuged at 4 °C at 12,000 rpm. The supernatant was collected and the total protein concentration was quantified using the BCA kit (Beyotime Biotechnology, P0010). The same amount of protein was loaded onto an SDS-PAGE gel and the isolated protein was transferred to a PVDF membrane. After sealing with 5% skimmed milk, the PVDF membrane was incubated with different types of primary antibodies (Table S4) for 2 h at room temperature, and the membrane was washed with TBST buffer three times for 0.5 h. Then, the membrane was incubated with HRP-conjugated secondary antibodies (Table S4) for 2 h at room temperature, and washed again with TBST buffer for 0.5 h. Finally, the membrane was scanned using an ECL system (BIO-RAD).

5.15. Cell Cycle Analysis. MDA-MB-231 cells were seeded at a density of 5×10^5 cells/well in six-well plates. Following overnight incubation, the cells were exposed to varying concentrations of ligand **5** for 48 h. Subsequently, trypsin was used to detach the cells, which were then harvested via centrifugation. The cells were fixed with 70% ethanol at 4 °C for 24 h. Following removal of the ethanol, the cells were washed three times with PBS and then incubated with 7-Aminoactinomycin D (Invitrogen, A1310) / RNase Staining Solution for 30 min at room temperature, protected from light. Finally, the cells were analyzed for cell cycle by means of flow cytometry using a BD Accuri C6 flow cytometer.

5.16. Study of DNA Damage with Comet Assay. Initially, 0.5% low melting point agarose (LMPA) was heated to 95°C, then cooled to 37 °C and set aside. Next, 10 μL of MDA-MB-231 cells (3000 cells) treated with different concentrations of ligand **5** and 75 μL of LMPA were mixed well at 37 °C, dropped quickly on the first layer of LMPA and covered evenly, and solidified at 4 °C for 10 min. The prepared slides were placed in lysis solution (2.5 mol/L NaCl, 100 mmol/L Na_2EDTA, 10 mmol/L Tris-HCl (pH = 10), 1% Triton X-100, 10% DMSO) and lysed at 4°C for 1.5 h. Later, they were transferred to a horizontal electrophoresis chamber with electrolyte (1 mmol/L Na_2EDTA, 300 mmol/L NaOH), and electrophoresis was performed at 300 mA for 20 min. Finally, the slides were removed and rinsed with PBS for 5 min, stained with DAPI for 10 min, and imaged on an inverted fluorescence microscope (Zeiss AX10). All procedures were executed in a dark room to prevent DNA damage caused by light.

5.17. hTERT Immunofluorescence Experiments in MDA-MB-231 Cells. MDA-MB-231 cells were treated with TBHP or **5**-TBHP complex for 48 hours. The cells were then fixed with 4% paraformaldehyde for 15 min, permeabilized with 0.1% Triton-X 100/PBS for 30 min at 37 °C, and closed with 1% BSA/PBS for 1 h. Immunofluorescence analyses were performed using standard methods. The samples were first incubated with hTERT primary antibody (HPA054641, Merck) for 2 h at 37 °C. After six washes with 1% BSA/PBS, the samples were incubated with Goat anti-Rabbit IgG (H+L) Cross-Adsorbed Secondary Antibody, Alexa Fluor 647 (SAB4600184, Merck) for 2 h at 37 °C. The samples were then washed three times with 1% BSA/PBS and stained with Hoechst 33342 for 10 min. Digital images were recorded with a Zeiss LSM 900 microscope (Hoechst, λ_{ex} = 405 nm, λ_{em} = 420–500 nm; Alexa Fluor 647, λ_{ex} = 640 nm, λ_{em} = 660–700 nm) and analyzed using ZEN software .

5.18. Reactive Oxygen Species (ROS) and Mitochondrial Membrane Potential (MMP) assays. MDA-MB-231 cells were inoculated on confocal dishes at a density of 5×10^5 cells/well. After overnight incubation, cells were treated with different concentrations of ligand **5** for 48 h, followed by Hoechst33342 for 1 h, and then stained with MitoSOX Mitochondrial Superoxide Indicators (Thermofisher Scientific, M36009), ROS Brite™ 670 (AAT Bioquest, 22903) or mitochondrial membrane potential dye (Thermofisher Scientific, M22425) for 30 min. After staining, cells were washed twice with DMEM complete medium, and finally the cells were subjected to confocal imaging under Zeiss LSM 900 microscope (Hoechst33342, λ_{ex} = 405 nm, λ_{em} = 420–500 nm; MitoSOX, λ_{ex} = 405 nm, λ_{em} =600–700 nm; ROS Brite™ 670, λ_{ex} = 640 nm, λ_{em} = 650–700 nm; mitochondrial membrane potential dye, λ_{ex} = 561 nm, λ_{em} = 640–700 nm) and analyzed using ZEN software.

5.19. Study of the Degree of Autophagy in Cells by Fluorescence Imaging. Cellular autophagy was detected using the MDC assay, where MDA-MB-231 cells were firstly inoculated in confocal dishes at a density of 5×10^5 cells/well, and after overnight incubation, the cells were treated with different concentrations of ligand **5** for 48 h. The cells were then incubated with MitoTracker Deep Red FM (Invitrogen, M22426) for 30 min, followed by the cellular autophagy staining assay with the kit for standard staining manipulation (Beyotime Biotechnology, C3018S). After staining, the cells were washed twice with DMEM complete medium, and finally the cells were subjected to confocal imaging under Zeiss LSM 900 microscope (MitoTracker Deep Red FM, λ_{ex} = 640 nm, λ_{em} = 650–700

nm; cellular autophagy kit C3018S, λ_{ex} = 405 nm, λ_{em} = 450–520 nm) and analyzed using ZEN software.

5.20. Study of Cellular Iron Metabolism by Fluorescence Imaging. MDA-MB-231 cells were inoculated in confocal dishes at a density of 5×10^5 cells overnight and treated with different concentrations of ligand 5 for 48 h. Cells were washed twice with DMEM complete medium, and then the cells were incubated with the Fe^{2+} probe FerroOrange (Merck, SCT210) and the nucleus probe Hoechst 33342 for 30 min. finally, cells were confocal imaged under a Zeiss LSM 900 microscope (Fe^{2+} probe, FerroOrange, λ_{ex} = 561 nm, λ_{em} = 570–600 nm; Hoechst 33342, λ_{ex} = 405 nm, λ_{em} = 420–500 nm) and analyzed using ZEN software.

5.21. Co-localization Experiments with Lysosomes and Mitochondria. MDA-MB-231 cells were inoculated in confocal dishes at a density of 5×10^5 cells/well, and after overnight incubation, the cells were treated with different concentrations of ligand **5** for 48 h. Then the cells were co-incubated with LysoTracker Blue DND-22 (Thermofisher Scientific, L7525) and MitoTracker Deep Red FM (Thermofisher Scientific, M22426) for 30 min and washed twice with DMEM complete medium at the end of staining. Finally, the cells were confocal imaged under a Zeiss LSM 900 microscope (LysoTracker Blue DND-22, λ_{ex} = 405 nm, λ_{em} = 420–480 nm; MitoTracker Deep Red FM, λ_{ex} = 640 nm, λ_{em} = 650–700 nm) and analyzed using ZEN software.

5.22. Transfection with pcDNA3.1 Containing hTERT Inserts. Plasmids pcDNA3.1(+)-C-eBFP and hTERT-pcDNA3.1(+)-C-eBFP containing inserts were designed. Transfection was performed using Lipofectamine 3000 (Thermofisher Scientific) and Opti MEM (Thermofisher Scientific), and the transfection process was carried out according to the protocol provided by the manufacturer. Briefly, MDA-MB-231 cells were inoculated into the 96-well and 6-well plates according to the manufacturer's instructions. After overnight incubation, two 1.5 mL Eppendorf tubes were prepared: Lipofectamine 3000 (tube 1) was diluted with Opti MEM, plasmid pcDNA3.1(+)-C-eBFP or hTERT-pcDNA3.1(+)-C-eBFP was diluted with Opti MEM and P3000 reagent was added (tube 2). The volumes of all reagents have been made up according to the manufacturer's instructions. Transfer 2 tubes of solution to 1 tube and mix thoroughly, incubate at room temperature for 15 min. Add the mixed solution to the well containing MDA-MB-231 cells for transfection. After 48 h of transfection, the cells were observed by laser confocal microscopy (λ_{ex} = 405 nm, λ_{em} = 420–500 nm) to assess the transfection efficiency.

5.23. Seahorse Experiment. In mitochondrial stress test experiment, MDA-MB-231 cells in DMEM were inoculated at a density of 4×10^4 cells/well in 24-well Agilent Seahorse XF cell culture microplate (Agilent Technologies) for 24 h, and then the cells were incubated for 2 h with different concentrations of **5**. Calibration was performed with 1 mL of Agilent Seahorse XF Calibration Solution (Agilent Technologies), and the calibration plates were placed in a CO_2-free incubator at 37 °C overnight. DMEM was then removed from the microplate and 500 μL of assay medium (DEME Assay Medium provided by Agilent Technologies with 1 mM pyruvate, 2 mM glutamine and 10 mM d-glucose, pH=7.4 at 37 °C) was added. The microplate with cells were placed in a CO_2-free incubator at 37 °C for 1 h. In addition, the sensor cartridges on the calibration plates were loaded with different compounds (port A: 56 μL of 1.5 μM oligomycin; port B: 62 μL of 1 μM FCCP; port C: 69 μL of 0.5 μM rotenone and 0.5 μM antimycin A). The sensor cartridges loaded on the microplate were placed in the XF24 analyzer (Agilent Technologies) for 30 min. after incubation, the calibration plate was replaced with the microplate with cells. In the glycolytic rate test experiment, except for the assay medium (DEME assay medium supplied by Agilent Technologies with 2 mM glutamine, pH=7.4 at 37 °C) and the loading of compounds in the sensor cassettes on the calibration plates (port A: 56 μL 10 mM glucose; port B: 62 μL of 1 μM oligomycin; port C: 69 μL of 50 mM 2-DG) were different from the mitochondrial stress test, other experimental conditions were consistent. Mitochondrial stress test and glycolytic rate test were performed using Seahorse software Wave.

5.24. mRNA Sequencing Analysis for MDA-MB-231 Cells Treated with Ligand 5. MDA-MB-231 cells were seeded at density 1×10^5 cells/flask in a 25-cm^2 culture flask. After overnight incubation, the cells were treated with 1 μM ligand **5** for 48 h. After treatment, extraction of RNA from cells using the RNase Mini kit (Qiagen). After that, the RNA samples were sent to Novogene company for RNA sequencing and data analysis. The raw transcriptome data have been deposited in NCBI Sequence Read Archive (SRA) database (BioProject: PRJNA1080090). Briefly, the quantity and quality of RNA samples were assessed by Qubit 4.0 fluorometer (ThermoFisher Scientific) and Agilent 2100 Bioanalyzer (Agilent) respectively. cDNA libraries were prepared from RNA samples with Illumina TruSeq Stranded Total RNA Prep kit (ligation with Ribo-Zero Plus) and indexing kit (Illumina). The quantity and quality of prepared cDNA libraries were assessed by Qubit 4.0 fluorometer and Agilent 2100 Bioanalyzer respectively. The cDNA libraries of experimental and control groups were pooled, and the sequencing was done by Illumina NextSeq 6000 system with

150bp paired-end dual-indexed method. The sequencing quality of the experimental and control samples was determined by FastQC. The low-quality reads and adapter sequences were trimmed with Fastp. The trimmed reads were further aligned to human reference genome (GRCh38/hg38) with STAR package (R programming). The STAR output (reads per gene) was subjected to DESeq2 (R programming) to perform differential expression analysis. Genes with fold-change>2 or <−2 and p-value <0.05 were defined as differentially expressed genes. By this criterion, a heat map of expression patterns was generated in R (pheatmap). Differentially expressed genes (DEGs) analysis was performed using DESeq2, and volcano maps were drawn based on the results of differential analysis. Gene Ontology (GO) enrichment analysis using topGO and Kyoto Encyclopedia of Genes and Genomes (KEGG) pathway enrichment analysis using clusterProfiler were performed for DEGs. Gene Set Enrichment Analysis (GSEA) was carried out using the clusterProfiler software with hallmark gene sets (H collection) and canonical pathways gene sets (CP in C2 collection) in Molecular Signatures Database (MSigDB 7.2).

5.25. *In Vivo* Antitumor Treatment. All animal experiments were performed in compliance with the Rules for the Management of Animals of the Ministry of Health of the People's Republic of China. All animal experiments performed in this study were in accordance with the animal welfare regulations and guidelines of the Institutional Ethics Committee. All animal care and procedures were approved by the University Ethics Committee for use with experimental animals. The approved ASESC (Animal Subjects Ethics Sub-Committee) Case number is 21-22/45-ABCT-R-GRF. Experiments were performed with 2% isoflurane to minimize suffering. In this study, female Balb/c nude mice (18–20 g) were placed in small animal isolators under sterile conditions to have free access to food and water. To establish a xenograft model, the MDA-MB-231 cell suspension (5×10^6 cells) was injected subcutaneously. When the subcutaneous tumor diameter was 100 mm^3, female nude mice were divided into three groups: tail vein injection of PBS, tail vein injection of ligand **5** (2 mg/kg), and tail vein injection of ligand **5** (5 mg/kg). Mice were executed on the 16^{th} day after intravenous injection of ligand **5** or PBS every two days, blood samples were collected and centrifuged to separate into cell and serum fractions for blood biochemical data analyzed, and major organs and tumor tissues were taken from each group for hematoxylin and eosin (H&E) staining, TUNEL staining, and Ki67 staining.

5.26. Statistical Analysis. Statistical details including the number of biological replicates (N) and P values are detailed in figure legends. Data in bar graphs are shown as an absolute number with means ± SD noted. Wilcoxon-Mann-Whitney test was used to calculate significant differences where indicated. $P < 0.05$ was considered statistically significant; ns, not significant. The criterion for statistical significance was taken as ns: $p > 0.05$, (*) $P < 0.05$, (**) $P < 0.01$, and (***) $P < 0.001$.

5.27. Data Availability. The main data supporting the results in this study are available within the paper and Supplementary Information. The raw and analyzed datasets generated during the study are too large to be publicly shared but are available for research purposes from the corresponding authors on reasonable request.

ASSOCIATED CONTENT

Supporting Information

The Supporting Information is available free of charge at

Experimental conditions, supplementary figures and tables for the results associated with the paper (PDF).

Molecular string files for all of the final target compounds (CSV).

AUTHOR INFORMATION

Corresponding Author

Yu-Jing Lu − School of Biomedical and Pharmaceutical Sciences, Guangdong University of Technology, Guangzhou 510006, P. R. China; Email: luyj@gdut.edu.cn

Chunyang Cao − State Key Laboratory of Chemical Biology, Shanghai Institute of Organic Chemistry, Chinese Academy of Sciences, 345 Lingling Road, Shanghai, 200032, P. R. China; ccao@mail.sioc.ac.cn

Wing-Leung Wong − State Key Laboratory of Chemical Biology and Drug Discovery, Department of Applied Biology and Chemical Technology, The Hong Kong Polytechnic University, Hung Hom, Kowloon, Hong Kong SAR 999077, China. orcid.org/0000-0001-7191-7578; Email: wing.leung.wong@polyu.edu.hk

Authors

Wei Long − State Key Laboratory of Chemical Biology and Drug Discovery, Department of Applied Biology and Chemical Technology, The Hong Kong Polytechnic University, Kowloon, Hong Kong SAR 999077, China

Yao-Xun Zeng − State Key Laboratory of Chemical Biology and Drug Discovery, Department of Applied Biology and Chemical Technology, The Hong Kong Polytechnic University, Kowloon, Hong Kong SAR 999077, China

Bo-Xin Zheng − State Key Laboratory of Chemical Biology and Drug Discovery, Department of Applied Biology and Chemical Technology, The Hong Kong Polytechnic University, Kowloon, Hong Kong SAR 999077, China

Yu-Bo Li − State Key Laboratory of Chemical Biology, Shanghai Institute of Organic Chemistry, Chinese Academy of Sciences, 345 Lingling Road, Shanghai, 200032, P. R. China

Ya-Kun Wang − State Key Laboratory of Chemical Biology and Drug Discovery, Department of Applied Biology and Chemical Technology, The Hong Kong Polytechnic University, Kowloon, Hong Kong SAR 999077, China

Ka-Hin Chan − State Key Laboratory of Chemical Biology and Drug Discovery, Department of Applied Biology and Chemical Technology, The Hong Kong Polytechnic University, Kowloon, Hong Kong SAR 999077, China

Meng-Ting She − State Key Laboratory of Chemical Biology and Drug Discovery, Department of Applied Biology and Chemical Technology, The Hong Kong Polytechnic University, Kowloon, Hong Kong SAR 999077, China

Author Contributions

All authors contributed equally in the present study.

Notes

The authors declare no competing financial interest.

ACKNOWLEDGMENTS

This work is fully supported by a grant from the Research Grants Council of the Hong Kong Special Administrative Region, China (RGC Project No. 15300522) and PolyU SZRI Fund (No. P0039278). W.L. acknowledges the award of a postdoctoral fellowship administered by the Research Committee of The Hong Kong Polytechnic University. We acknowledged Dr. Chan Chun-ming, Fortune, Scientific Officer of the Deparatment of Applied Biology and Chemical Biology, The Hong Kong Polytechnic University, for his kind assistance provided in the NMR study. The University Research Facilities on Life Sciences of The Hong Kong Polytechnic University.

ABBREVIATIONS

2-DG, 2-deoxy-D-glucose; BRACO19, N,N'-(9-((4-(dimethylamino)phenyl)amino)acridine-3,6-diyl)bis(3-(pyrrolidin-1-yl)propanamide); eBFP, enhanced blue fluorescent protein; FBS, fetal bovine serum; FCCP, Trifluoromethoxy carbonylcyanide phenylhydrazone; G4s, G-quadruplex structure; GTC365, 3-guanidino-N-(4-((3-nitroacridin-9-yl)amino)phenyl)propane-1-sulfonamide; Hoechst33342, 2′-(4-ethoxyphenyl)-6-(4-methylpiperazin-1-yl)-1H,3′H-2,5′-bibenzo[d]imidazole; MTT, 3-(4,5-dimethylthiazol-2-yl)-2,5-diphenyltetrazolium bromide; PBS, phosphate-buffered saline; RHPS4, 3,11-difluoro-6,8,13-trimethyl-8H-quinolino[4,3,2-kl]acridin-13-ium methyl sulfate; SOP1812, 2,7-bis(3-morpholinopropyl)-4-((2-(pyrrolidin-1-yl)ethyl)amino)-9-(4-(pyrrolidin-1-ylmethyl)phenyl)benzo[lmn][3,8]phenanthroline-1,3,6,8(2H,7H)-tetraone; TMPyP4, 5,10,15,20-tetrakis(N-methyl-4-pridyl)porphyrine; TRAP, Telomerase Repeated Amplification Protocol.

REFERENCES

(1) Aubert, G.; Lansdorp, P. M. Telomeres and aging. *Physiol. Rev.* **2008**, *88*, 557–579.

(2) Shay, J. W. Role of Telomeres and Telomerase in Aging and Cancer. *Cancer Discov.* **2016**, *6*, 584–593.

(3) Akincilar, S. C.; Unal, B.; Tergaonkar, V. Reactivation of telomerase in cancer. *Cell. Mol. Life Sci.* **2016**, *73*, 1659–1670.

(4) Shay, J. W.; Wright, W. E. Senescence and immortalization: role of telomeres and telomerase. *Carcinogenesis* **2005**, *26*, 867–874.

(5) Del Bufalo, D.; Rizzo, A.; Trisciuoglio, D.; Cardinali, G.; Torrisi, M. R.; Zangemeister-Wittke, U.; Zupi, G.; Biroccio, A. Involvement of hTERT in apoptosis induced by interference with Bcl-2 expression and function. *Cell Death. Differ.* **2005**, *12*, 1429–1438.

(6) Masutomi, K.; Possemato, R.; Wong, J. M. Y.; Currier, J. L.; Tothova, Z.; Manola, J. B.; Ganesan, S.; Lansdorp, P. M.; Collins, K.; Hahn, W. C. The telomerase reverse transcriptase regulates chromatin state and DNA damage responses. *Proc. Natl. Acad. Sci. U. S. A.* **2005**, *102*, 8222–8227.

(7) Shin, K. H.; Kang, M. K.; Dicterow, E.; Kameta, A.; Baluda, M. A.; Park, N. H. Introduction of human telomerase reverse transcriptase to normal human fibroblasts enhances DNA repair capacity. *Clin. Cancer Res.* **2004**, *10*, 2551–2560.

(8) Haendeler, J.; Dröse, S.; Büchner, N.; Jakob, S.; Altschmied, J.; Goy, C.; Spyridopoulos, I.; Zeiher, A. M.; Brandt, U.; Dimmeler, S. Mitochondrial Telomerase Reverse Transcriptase Binds to and Protects Mitochondrial DNA and Function From Damage. *Arteriosclerosis Thrombosis and Vascular Biology* **2009**, *29*, 929–935.

(9) Romaniuk-Drapala, A.; Toton, E.; Konieczna, N.; Machnik, M.; Barczak, W.; Kowal, D.; Kopczynski, P.; Kaczmarek, M.; Rubis, B. hTERT Downregulation Attenuates Resistance to DOX, Impairs FAK-Mediated Adhesion, and Leads to Autophagy Induction in Breast Cancer Cells. *Cells* **2021**, *10*, 867.

(10) Liu, Y.; Betori, R. C.; Pagacz, J.; Frost, G. B.; Efimova, E. V.; Wu, D.; Wolfgeher, D. J.; Bryan, T. M.; Cohen, S. B.; Scheidt, K. A.; Kron, S. J. Targeting telomerase reverse transcriptase with the covalent inhibitor NU-1 confers immunogenic radiation sensitization. *Cell Chem. Biol.* **2022**, *29*, 1517–1531.

(11) Gay-Bellile, M.; Véronèse, L.; Combes, P.; Eymard-Pierre, E.; Kwiatkowski, F.; Dauplat, M. M.; Cayre, A.; Privat, M.; Abrial, C.; Bignon, Y. J.; Mouret-Reynier, M. A.; Vago, P.; Penault-Llorca, F.; Tchirkov, A. TERT promoter status and gene copy number gains: effect on TERT expression and association with prognosis in breast cancer. *Oncotarget* **2017**, *8*, 77540–77551.

(12) Vinagre, J.; Almeida, A.; Pópulo, H.; Batista, R.; Lyra, J.; Pinto, V.; Coelho, R.; Celestino, R.; Prazeres, H.; Lima, L.; Melo, M.; Rocha, A. G.; Preto, A.; Castro, P.; Castro, L.; Pardal, F.; Lopes, J. M.; Santos, L. L.; Reis, R. M.; Cameselle-Teijeiro, J.; Sobrinho-Simões, M.; Lima, J.;

Máximo, V.; Soares, P. Frequency of TERT promoter mutations in human cancers. *Nat. Commun.* **2013**, *4*, 2185.

(13) Guilleret, I.; Yan, P.; Grange, F.; Braunschweig, R.; Bosman, F. T.; Benhattar, J. Hypermethylation of the human telomerase catalytic subunit (hTERT) gene correlates with telomerase activity. *Int. J. Cancer* **2002**, *101*, 335–341.

(14) Castelo-Branco, P.; Choufani, S.; Mack, S.; Gallagher, D.; Zhang, C.; Lipman, T.; Zhukova, N.; Walker, E. J.; Martin, D.; Merino, D.; Wasserman, J. D.; Elizabeth, C.; Alon, N.; Zhang, L.; Hovestadt, V.; Kool, M.; Jones, D. T. W.; Zadeh, G.; Croul, S.; Hawkins, C.; Hitzler, J.; Wang, J. C. Y.; Baruchel, S.; Dirks, P. B.; Malkin, D.; Pfister, S.; Taylor, M. D.; Weksberg, R.; Tabori, U. Methylation of the TERT promoter and risk stratification of childhood brain tumor s: an integrative genomic and molecular study. *Lancet Oncol.* **2013**, *14*, 534–542.

(15) Castelo-Branco, P.; Leao, R.; Lipman, T.; Campbell, B.; Lee, D.; Price, A.; Zhang, C.; Heidari, A.; Stephens, D.; Boerno, S.; Coelho, H.; Gomes, A.; Domingos, C.; Apolonio, J. D.; Schäfer, G.; Bristow, R. G.; Schweiger, M. R.; Hamilton, R.; Zlotta, A.; Figueiredo, A.; Klocker, H.; Sü ltmann, H.; Tabori, U. A cancer specific hypermethylation signature of the TERT promoter predicts biochemical relapse in prostate cancer: A retrospective cohort study. *Oncotarget* **2016**, *7*, 57726–57736.

(16) Leao, R.; Apolónio, J. D.; Lee, D.; Figueiredo, A.; Tabori, U.; Castelo-Branco, P. Mechanisms of human telomerase reverse transcriptase (hTERT) regulation: clinical impacts in cancer. *J. Biomed. Sci.* **2018**, *25*, 22.

(17) Lassmann, T.; Maida, Y.; Tomaru, Y.; Yasukawa, M.; Ando, Y.; Kojima, M.; Kasim, V.; Simon, C.; Daub, C. O.; Carninci, P.; Hayashizaki, Y.; Masutomi, K. Telomerase Reverse Transcriptase Regulates microRNAs. *Int. J. Mol. Sci.* **2015**, *16*, 1192–1208.

(18) Shanmugaraj, B.; Priya, L. B.; Mahalakshmi, B.; Subbiah, S.; Hu, R. M.; Velmurugan, B. K.; Baskaran, R. Bacterial and viral vectors as vaccine delivery vehicles for breast cancer therapy. *Life Sci.* **2020**, *250*, 117550.

(19) Ohira, T.; Naohiro, S.; Nakayama, Y.; Osaki, M.; Okada, F.; Oshimura, M.; Kugoh, H. miR-19b regulates hTERT mRNA expression through targeting PITX1 mRNA in melanoma cells. *Sci. Rep.* **2015**, *5*, 8201.

(20) El-Desoky, A. M.; Ali, Y. B. M.; Talaat, R. M. Cytotoxic effect of combining two antisense oligonucteotides against telomerase rna component (hTR and mRNA of centromere protein B (CENP-B) in hepatocellutar carcinoma cells. *An. Acad. Bras. Cienc.* **2022**, *94*, e20200573.

(21) Hunger, R. E.; Lang, K. K.; Markowski, C. J.; Trachsel, S.; Moller, M.; Eriksen, J. A.; Rasmussen, A. M.; Braathen, L. R.; Gaudernack, G. Vaccination of patients with cutaneous melanoma with telomerase-specific peptides. *Cancer Immunol. Immunother.* **2011**, *60*, 1553–1564.

(22) Fenoglio, D.; Parodi, A.; Lavieri, R.; Kalli, F.; Ferrera, F.; Tagliamacco, A.; Guastalla, A.; Lamperti, M. G.; Giacomini, M.; Filaci, G. Immunogenicity of GX301 cancer vaccine: Four (telomerase peptides) are better than one. *Hum. Vaccin. Immunother.* **2015**, *11*, 838–850.

(23) Pascolo, E.; Wenz, C.; Lingner, J.; Hauel, N.; Priepke, H.; Kauffmann, I.; Garin-Chesa, P.; Rettig, W. J.; Damm, K.; Schnapp, A. Mechanism of human telomerase inhibition by BIBR1532, a synthetic, non-nucleosidic drug candidate. *J. Biol. Chem.* **2002**, *277*, 15566–15572.

(24) Samad, M. A.; Saiman, M. Z.; Majid, N. A.; Karsani, S. A.; Yaacob, J. S. Berberine Inhibits Telomerase Activity and Induces Cell Cycle Arrest and Telomere Erosion in Colorectal Cancer Cell Line, HCT 116. *Molecules* **2021**, *26*, 376.

(25) Wang, Q.; Liu, J. Q.; Chen, Z.; Zheng, K. W.; Chen, C. Y.; Hao, Y. H.; Tan, Z. G-quadruplex formation at the 3' end of telomere DNA inhibits its extension by telomerase, polymerase and unwinding by helicase. *Nucleic Acids Res.* **2011**, *39*, 6229–6237.

(26) Bay, D. H.; Busch, A.; Lisdat, F.; Iida, K.; Ikebukuro, K.; Nagasawa, K.; Karube, I.; Yoshida, W. Identification of G-quadruplex structures that possess transcriptional regulating functions in the Dele and Cdc6 CpG islands. *BMC Mol. Biol.* **2017**, *18*, 17.

(27) Jodoin, R.; Carrier, J. C.; Rivard, N.; Bisaillon, M.; Perreault, J. P. G-quadruplex located in the 5′UTR of the BAG-1 mRNA affects both its cap-dependent and cap-independent translation through global secondary structure maintenance. *Nucleic Acids Res.* **2019**, *47*, 10247–10266.

(28) Palumbo, S. L.; Ebbinghaus, S. W.; Hurley, L. H. Formation of a Unique End-to-End Stacked Pair of G-Quadruplexes in the hTERT Core Promoter with Implications for Inhibition of Telomerase by G-Quadruplex-Interactive Ligands. *J. Am. Chem. Soc.* **2009**, *131*, 10878–10891.

(29) Lim, K. W.; Lacroix, L.; Yue, D. J. E.; Lim, J. K. C.; Lim, J. M. W.; Phan, A. T. Coexistence of Two Distinct G-Quadruplex Conformations in the hTERT Promoter. *J. Am. Chem. Soc.* **2010**, *132*, 12331–12342.

(30) Kang, H. J.; Cui, Y. X.; Yin, H.; Scheid, A.; Hendricks, W. P. D.; Schmidt, J.; Sekulic, A.; Kong, D. M.; Trent, J. M.; Gokhale, V.; Mao, H.; Hurley, L. H. A Pharmacological Chaperone Molecule Induces Cancer Cell Death by Restoring Tertiary DNA Structures in Mutant hTERT Promoters. *J. Am. Chem. Soc.* **2016**, *138*, 13673–13692.

(31) Monsen, R. C.; DeLeeuw, L.; Dean, W. L.; Gray, R. D.; Sabo, T. M.; Chakravarthy, S.; Chaires, J. B.; Trent, J. O. The hTERT core promoter forms three parallel G-quadruplexes. *Nucleic Acids Res.* **2020**, *48*, 5720–5734.

(32) Pavlova, A. V.; Savitskaya, V. Y.; Dolinnaya, N. G.; Monakhova, M. V.; Litvinova, A. V.; Kubareva, E. A.; Zvereva, M. I. G-Quadruplex Formed by the Promoter Region of the hTERT Gene: Structure-Driven Effects on DNA Mismatch Repair Functions. *Biomedicines* **2022***, 10*, 1871.

(33) Saha, D.; Singh, A.; Hussain, T.; Srivastava, V.; Sengopta, S.; Kar, A.; Dhapola, P.; Dhople, V.; Unnmanni, R.; Chowdhury, S. Epigenetic suppression of human telomerase (hTERT) is mediated by the metastasis suppressor NME2 in a G-quadruplex-dependent fashion. *J. Biol. Chem.* **2017**, *292*, 15205–15215.

(34) Grand, C. L.; Han, H. Y.; Muñoz, R. M.; Weitman, S.; Von Hoff, D. D.; Hurley, L. H.; Bearss, D. J. The cationic porphyrin TMPyP4 down-regulates c-MYC and human telomerase reverse transcriptase expression and inhibits tumor growth in vivo. *Mol. Cancer Ther.* **2002**, *1*, 565–573.

(35) Kim, M. Y.; Vankayalapati, H.; Kazuo, S.; Wierzba, K.; Hurley, L. H. Telomestatin, a potent telomerase inhibitor that interacts quite specifically with the human telomeric intramolecular G-quadruplex. *J. Am. Chem. Soc.* **2002**, *124*, 2098–2099.

(36) Zhou, G. T.; Liu, X. R.; Li, Y. Q.; Xu, S. B.; Ma, C. Y.; Wu, X. M.; Cheng, Y.; Yu, Z. Y.; Zhao, G.; Chen, Y. Telomere targeting with a novel G-quadruplex-interactive ligand BRACO-19 induces T-loop disassembly and telomerase displacement in human glioblastoma cells. *Oncotarget* **2016***, 7*, 14925–14939.

(37) Lipps, H. J.; Rhodes, D. G-quadruplex structures: in vivo evidence and function. *Trends. Cell Biol.* **2009**, *19*, 414–422.

(38) Song, J. H.; Kang, H. J.; Luevano, L. A.; Gokhale, V.; Wu, K.; Pandey, R.; Chow, H. H. S.; Hurley, L. H.; Kraft, A. S. Small-Molecule-Targeting Hairpin Loop of hTERT Promoter G-Quadruplex Induces Cancer Cell Death. *Cell Chem. Biol.* **2019**, *26*, 1110–1121.

(39) Ahmed, A. A.; Angell, R.; Oxenford, S.; Worthington, J.; Williams, N.; Barton, N.; Fowler, T. G.; O'Flynn, D. E.; Sunose, M.; McConville, M.; Vo, T.; Wilson, W. D.; Karim, S. A.; Morton, J. P.; Neidle, S. Asymmetrically Substituted Quadruplex-Binding Naphthalene Diimide Showing Potent Activity in Pancreatic Cancer Models. *ACS Med. Chem. Lett.* **2020**, *11*, 1634–1644.

(40) Long, W.; Zheng, B. X.; Huang, X. H.; She, M. T.; Liu, A. L.; Zhang, K.; Wong, W. L.; Lu, Y. J. Molecular Recognition and Imaging of Human Telomeric G-Quadruplex DNA in Live Cells: A Systematic Advancement of Thiazole Orange Scaffold To Enhance Binding Specificity and Inhibition of Gene Expression. *J. Med. Chem.* **2021***, 64*, 2125–2138.

(41) Long, W.; Zheng, B. X.; Li, Y.; Huang, X. H.; Lin, D. M.; Chen, C. C.; Hou, J. Q.; Ou, T. M.; Wong, W. L.; Zhang, K.; Lu, Y. J. Rational design of small-molecules to recognize G-quadruplexes of c-MYC promoter and telomere and the evaluation of their *in vivo* antitumor activity against breast cancer. *Nucleic Acids Res.* **2022**, *50*, 1829–1848.

(42) Feigon, J.; Koshlap, K. M.; Smith, F. W. 1H NMR spectroscopy of DNA triplexes and quadruplexes. *Methods. Enzymol.* **1995**, *261*, 225–255.

(43) Phan, A. T.; Kuryavyi, V.; Gaw, H. Y.; Patel, D. J. Small-molecule interaction with a five-guanine-tract G-quadruplex structure from the human MYC promoter. *Nat. Chem. Biol.* **2005**, *1*, 167–173.

(44) Cesare, A. J.; Reddel, R. R. Alternative lengthening of telomeres: models, mechanisms and implications. *Nat. Rev. Genet.* **2010**, *11*, 319–330.

(45) Biffi, G.; Tannahill, D.; McCafferty, J.; Balasubramanian, S. Quantitative visualization of DNA G-quadruplex structures in human cells. *Nat. Chem.* **2013**, *5*, 182–186.

(46) Yang, R. Z.; Han, Y.; Guan, X. Y.; Hong, Y.; Meng, J. H.; Ding, S. R.; Long, Q.; Yi, W. J. Regulation and clinical potential of telomerase reverse transcriptase (TERT/hTERT) in breast cancer. *Cell Commun. Signal.* **2023**, *21*, 218.

(47) Ong, C. T.; Corces, V. G. CTCF: an architectural protein bridging genome topology and function. *Nat. Rev. Genet.* **2014**, *15*, 234–246.

(48) Muñoz, P.; Blanco, R.; Blasco, M. A. Role of the TRF2 telomeric protein in cancer and ageing. *Cell Cycle* **2006**, *5*, 718-721.

(49) Jafri, M. A.; Ansari, S. A.; Alqahtani, M. H.; Shay, J. W. Roles of telomeres and telomerase in cancer, and advances in telomerase-targeted therapies. *Genome Med.* **2016**, *8*, 69.

(50) Dratwa, M.; Wysoczanska, B.; Lacina, P.; Kubik, T.; Bogunia-Kubik, K. TERT-Regulation and Roles in Cancer Formation. *Front. Immunol.* **2020**, *11*, 589929.

(51) Kumari, R.; Jat, P. Mechanisms of Cellular Senescence: Cell Cycle Arrest and Senescence Associated Secretory Phenotype. *Front. Cell. Dev. Biol.* **2021**, *9*, 645593.

(52) Kalsbeek, D.; Golsteyn, R. M. G2/M-Phase Checkpoint Adaptation and Micronuclei Formation as Mechanisms That Contribute to Genomic Instability in Human Cells. *Int. J. Mol. Sci.* **2017**, *18*, 2344.

(53) Riceevans, C.; Baysal, E.; Pashby, D. P.; Hochstein, P. t-butyl hydroperoxide-induced perturbations of human erythrocytes as a model for oxidant stress. *Biochim. Biophys. Acta* **1985**, *815*, 426–432.

(54) Green, D. R.; Galluzzi, L.; Kroemer, G. Mitochondria and the Autophagy-Inflammation-Cell Death Axis in Organismal Aging. *Science* **2011**, *333*, 1109–1112.

(55) Novak, I.; Kirkin, V.; McEwan, D. G.; Zhang, J.; Wild, P.; Rozenknop, A.; Rogov, V.; Löhr, F.; Popovic, D.; Occhipinti, A.; Reichert, A. S.; Terzic, J.; Dötsch, V.; Ney, P. A.; Dikic, I. Nix is a selective autophagy receptor for mitochondrial clearance. *EMBO Rep.* **2010**, *11*, 45–51.

(56) Geisler, S.; Holmström, K. M.; Skujat, D.; Fiesel, F. C.; Rothfuss, O. C.; Kahle, P. J.; Springer, W. PINK1/Parkin-mediated mitophagy is dependent on VDAC1 and p62/SQSTM1. *Nature Cell Biology* **2010**, *12*, 119–131.

(57) Schaaf, M. B. E.; Keulers, T. G.; Vooijs, M. A.; Rouschop, K. M. A. LC3/GABARAP family proteins: autophagy-(un) related functions. *FASEB J.* **2016**, *30*, 3961–3978.

(58) Rikka, S.; Quinsay, M. N.; Thomas, R. L.; Kubli, D. A.; Zhang, X.; Murphy, A. N.; Gustafsson, Å. Bnip3 impairs mitochondrial bioenergetics and stimulates mitochondrial turnover. *Cell Death. Differ.* **2011**, *18*, 721–731.

(59) Narendra, D. P.; Kane, L. A.; Hauser, D. N.; Fearnley, I. M.; Youle, R. J. p62/SQSTM1 is

required for Parkin-induced mitochondrial clustering but not mitophagy; VDAC1 is dispensable for both. *Autophagy* **2010**, *6*, 1090–1106.

(60) Liu, J.; Kuang, F. M.; Kroemer, G.; Klionsky, D. J.; Kang, R.; Tang, D. L. Autophagy-Dependent Ferroptosis: Machinery and Regulation. *Cell Chem. Biol.* **2020**, *27*, 420–435.

(61) Xie, Y. C.; Kang, R.; Klionsky, D. J.; Tang, D. L. GPX4 in cell death, autophagy, and disease. *Autophagy* **2023**, *19*, 2621–2638.

(62) van der Vos, K. E.; Eliasson, P.; Proikas-Cezanne, T.; Vervoort, S. J.; van Boxtel, R.; Putker, M.; van Zutphen, I. J.; Mauthe, M.; Zellmer, S.; Pals, C.; Verhagen, L. P.; Koerkamp, M.; Braat, A. K.; Dansen, T. B.; Holstege, F. C.; Gebhardt, R.; Burgering, B. M.; Coffer, P. J. Modulation of glutamine metabolism by the PI(3)K-PKB-FOXO network regulates autophagy. *Nat. Cell Biol.* **2012**, *14*, 829–837.

(63) Pannunzio, N. R.; Watanabe, G.; Lieber, M. R. Nonhomologous DNA end-joining for repair of DNA double-strand breaks. *J. Biol. Chem.* **2018**, *293*, 10512–10523.

(64) Ying, W. H. NAD^+/NADH and $NADP^+$/NADPH in cellular functions and cell death: Regulation and biological consequences. *Antioxid. Redox Signal.* **2008**, *10*, 179–206.

(65) Marinaccio, J.; Micheli, E.; Udroiu, I.; Di Nottia, M.; Carrozzo, R.; Baranzini, N.; Grimaldi, A.; Leone, S.; Moreno, S.; Muzzi, M.; et al. TERT Extra-Telomeric Roles: Antioxidant Activity and Mitochondrial Protection. *International Journal of Molecular Sciences* **2023**, *24*, 21.

Table of Contents Graphic